

2.02

Seismological Constraints upon Mantle Composition

C. R. Bina

Northwestern University, Evanston, IL, USA

2.02.1	INTRODUCTION	39
2.02.1.1	<i>General Considerations</i>	39
2.02.1.2	<i>Bulk Sound Velocity</i>	40
2.02.1.3	<i>Acoustic Methods</i>	40
2.02.2	UPPER-MANTLE BULK COMPOSITION	41
2.02.2.1	<i>Overview</i>	41
2.02.2.2	<i>Velocity Contrasts</i>	42
2.02.2.3	<i>Discontinuity Topography</i>	42
2.02.2.4	<i>Sharpness</i>	43
2.02.2.5	<i>Broadening and Bifurcation</i>	43
2.02.3	UPPER-MANTLE HETEROGENEITY	45
2.02.3.1	<i>Subducted Basalts</i>	45
2.02.3.2	<i>Plume Origins</i>	46
2.02.4	LOWER-MANTLE BULK COMPOSITION	48
2.02.4.1	<i>Bulk Fitting</i>	48
2.02.4.2	<i>Depthwise Fitting</i>	49
2.02.5	LOWER-MANTLE HETEROGENEITY	51
2.02.5.1	<i>Overview</i>	51
2.02.5.2	<i>Subducted Oceanic Crust</i>	52
2.02.6	SUMMARY	54
	REFERENCES	56

2.02.1 INTRODUCTION

2.02.1.1 General Considerations

Direct sampling of mantle rocks and minerals is limited to tectonic slices emplaced at the surface (see [Chapter 2.04](#)), smaller xenoliths transported upwards by magmatic processes (see [Chapter 2.05](#)), and still smaller inclusions in such far-traveled natural sample chambers as diamonds (see [Chapter 2.05](#)). Because of such limited direct access to mantle materials, knowledge of mantle structure, composition, and processes must be augmented by geophysical remote sensing. What can various seismological observations tell us about the major-element composition of the upper mantle? How can they constrain possible differences in chemical composition between the upper

and lower mantle? What light can they shed upon the nature of velocity heterogeneities in both the upper and lower mantle? It is these questions that we shall seek to address in this chapter.

Most seismological constraints on mantle composition are derived by comparison of values of seismic wave velocities inferred for particular regions within the Earth to the values measured in the laboratory for particular minerals or mineral assemblages, with such comparisons being made under comparable regimes of pressure (P) and temperature (T). The primary parameters of interest, then, are the compressional (or P -) wave velocities (V_P) and the shear (or S -) wave velocities (V_S). These wave velocities are simply related to the density (ρ) and to the two isotropic elastic moduli, the adiabatic bulk modulus (K_S)

and the shear (or “rigidity”) modulus (G), via $V_P^2 = [K_S + (4/3)G]/\rho$ and $V_S^2 = G/\rho$, respectively.

2.02.1.2 Bulk Sound Velocity

Straightforward measurements of elastic properties of materials can be made via high-pressure static compression experiments, in which X-ray diffraction (XRD) is used to measure the molar volume (V), or equivalently the density (ρ), of a material as a function of pressure (P). The pressure dependence of volume is expressed by the “incompressibility” or isothermal bulk modulus (K_T), where $K_T = -V(\partial P/\partial V)_T$.

This isothermal bulk modulus (K_T) measured by static compression differs slightly from the aforementioned adiabatic bulk modulus (K_S) defining seismic velocities in that the former (K_T) describes resistance to compression at constant temperature, such as is the case in a laboratory device in which a sample is slowly compressed in contact with a large thermal reservoir such as the atmosphere. The latter (K_S), alternatively describes resistance to compression under adiabatic conditions, such as those pertaining when passage of a seismic wave causes compression (and relaxation) on a time-scale that is short compared to that of thermal conduction. Thus, the adiabatic bulk modulus generally exceeds the isothermal value (usually by a few percent), because it is more difficult to compress a material whose temperature rises upon compression than one which is allowed to conduct away any such excess heat, as described by a simple multiplicative factor $K_S = K_T(1 + T\alpha\gamma)$, where α is the volumetric coefficient of thermal expansion and γ is the thermodynamic Grüneisen parameter.

Experimentally, the bulk modulus is the simplest parameter to measure, but the seismological parameters of primary interest, V_P and V_S , both involve the shear modulus as well. It is convenient, therefore, to define a new parameter, the “bulk sound velocity” (V_ϕ), which eliminates all dependence upon the shear modulus (G) through a judicious linear combination of the squares of the two seismic wave velocities: $V_\phi^2 = K_S/\rho = V_P^2 - (4/3)V_S^2$. This new parameter (sometimes thought of as the P -wave velocity of an “equivalent” fluid, for which $G = 0$) can be determined directly from static compression data: $V_\phi^2 = K_S/\rho = (1 + T\alpha\gamma)(\partial P/\partial \rho)_T$. The bulk sound velocity possesses another desirable feature, in that it can also be constrained indirectly through chemical equilibrium experiments. Chemical equilibria describe free energy minima; the pressure dependence of free energy is described by the molar volume, and the pressure dependence of volume (or density) is described by K_T and hence V_ϕ . Thus, experimental determinations of equilibrium phase boundaries can

provide independent constraints upon V_ϕ (Bina and Helffrich, 1992).

Again, chemical composition in regions of Earth’s interior is primarily constrained by mapping values of seismic velocities in those regions and comparing the values to those determined for various candidate mineral assemblages. The primary observables in the seismological studies consist of measured travel times of various P - and S -waves, some of which can in principle constrain density contrasts (Shearer and Flanagan, 1999) from a large enough set of which values of V_P and V_S can be determined through mathematical inversion. Secondary observables include the measured amplitudes of various arriving P - and S -waves, some of which can in principle constrain density contrasts (Shearer and Flanagan, 1999) but these are much more sensitive to complex properties such as anelasticity than are simple travel times. Seismological observables, then, directly yield V_P and V_S , but static compression experiments directly yield V_ϕ . It is common, therefore, to seek to combine seismological V_P and V_S models to generate a V_ϕ model for a region, for comparison to mineralogically constrained V_ϕ values. Such combinatoric procedures can introduce additional errors, however, in that the V_P and V_S profiles used may often reflect seismic ray paths or frequency bands that differ from one another. Indeed, special source–receiver geometries (such as those whose epicentral distances are so small as to ensure nearly overlapping ray paths) may be necessary to obtain robust estimates of V_ϕ values (Bina and Silver, 1997). Nonetheless, comparisons to V_ϕ , rather than to V_P and V_S , are commonly used to constrain compositions in the deep interior, because (as noted below) mineralogical values for G (and hence for V_S) become more problematic with increasing depth.

2.02.1.3 Acoustic Methods

Direct laboratory measurements of V_P and V_S for materials can be made through acoustic methods, such as Brillouin spectroscopy and ultrasonic techniques. Brillouin spectroscopy (or “Brillouin scattering”) determines acoustic velocities in a single crystal through measurements of the Doppler shifts experienced by visible light scattering off the faces of a single crystal in which thermally induced acoustic waves are propagating. Because the technique employs single crystals, full elasticity tensors (rather than just isotropic V_P and V_S) can be determined, which are useful in studies of velocity anisotropy. The technique requires only small samples, and because visible light is employed, the samples may be placed in an optically transparent diamond-anvil cell (DAC) in order to make measurements at elevated pressures and temperatures. DAC studies yielding V_P and V_S may be

combined with XRD analyses yielding ρ , to allow for direct determination of K_S and G (and hence V_ϕ) for single crystals (Zha *et al.*, 1998a).

The second group of acoustic methods, the ultrasonic techniques, require larger samples but can be performed on either single crystals or polycrystalline aggregates. They require experimental measurement (via interferometry) of the travel times of two consecutive ultrasonic echoes from the ends of a shaped sample, combined with measurement of the length of the sample. These measurements directly yield V_P and V_S , rather than full anisotropic elasticity tensors, but this is usually sufficient (unless patterns of seismic velocity anisotropy are to be used to map strain fields in the mantle). Samples may be placed in a multi-anvil cell (MAC) to make measurements at elevated pressures and temperatures, and simultaneous (usually synchrotron) XRD analysis can then be used to keep track of associated changes in sample length. Again, MAC studies yielding V_P and V_S may be combined with ρ measurements from the XRD analyses to directly yield K_S and G (and hence V_ϕ) for samples (Li *et al.*, 2001).

The appealing flexibility of acoustic techniques is leading to rapid expansion of the regime of pressures and temperatures in which experimental measurements can be made. However, their potential utility continues to suffer from one poorly understood factor. While Brillouin and ultrasonic methods determine V_P and V_S at frequencies in the MHz–GHz range, seismological observations constrain V_P and V_S at frequencies in the mHz–Hz range. There is ample room for the poorly understood frequency dependence of these velocities (“dispersion”) potentially to confound petrological interpretations over these many orders of magnitude. Unhappily, V_S is much more subject to dispersion than is V_P , and the magnitude of such effects upon V_S (and hence G) only grows with increasing temperature (and hence depth). Thus, until V_S values can be both measured at simultaneous high P and T and extrapolated from GHz to mHz with confidence (and quantifiable error bounds), there remain important roles for the parameter V_ϕ . Not only does V_ϕ remain free of the dispersive and thermal complications of G , if determined in part by static compression methods it also benefits from being constrained by measurements near 0 Hz, closer to the seismic frequency band than acoustic techniques permit.

2.02.2 UPPER-MANTLE BULK COMPOSITION

2.02.2.1 Overview

Based upon the compositions of mantle rocks emplaced at the surface in large slices (see Chapter 2.04) or as small xenoliths (see Chapter 2.05),

the compositions of mantle-derived melts (see Chapter 2.08), various cosmochemical arguments (see Chapters 2.01 and 2.15), and simple geophysical considerations, the mineralogy of the upper mantle is commonly concluded to resemble that of some sort of peridotite (McDonough and Rudnick, 1998). Perhaps the most frequently invoked model composition is that of “pyrolite” (Ringwood, 1975, 1989), which contains ~60% olivine by volume, the depth-varying properties of which are dominated by progressive high-pressure phase transitions from olivine (α) to wadsleyite (β , also called “modified spinel”) to ringwoodite (γ , also called “silicate spinel”) and thence to a mixture of silicate perovskite (pv) and magnesiowüstite (mw, also called “ferropericlase”). The remaining, nonolivine, components are orthopyroxene (opx), clinopyroxene (cpx), and garnet (gt), and these undergo more gradual high-pressure transitions as the pyroxenes dissolve into the garnet, with the resulting “garnet–majorite” solid solution (gt–mj) eventually transforming to silicate perovskite as well (Figure 1). While this model of a peridotitic upper mantle has regularly been challenged, the proposed alternatives have

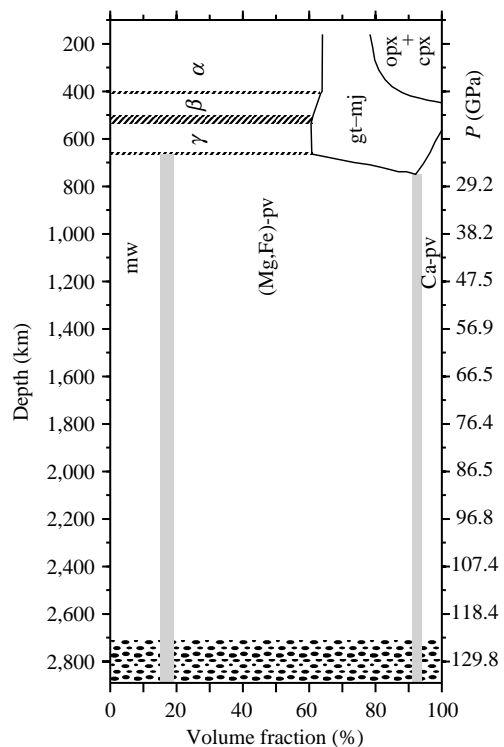


Figure 1 Depth-varying phase proportions in a pyrolite model mantle after the manner of Ringwood (1989), Ita and Stixrude (1992), and Bina (1998b). Phases are: (α) olivine, (β) wadsleyite, (γ) ringwoodite, (opx) orthopyroxene, (cpx) clinopyroxene, (gt–mj) garnet–majorite, (mw) magnesiowüstite, ((Mg,Fe)-pv) ferromagnesian silicate perovskite, and (Ca-pv) calcium silicate perovskite. Patterned region at base denotes likely heterogeneity near core–mantle boundary.

evolved over time to accommodate increasing quantities of olivine: from an eclogite containing little or no olivine (Anderson, 1979, 1982, 1984), through various “piclogite” models containing 16% (Bass and Anderson, 1984), 22% (Anderson and Bass, 1984), 30% (Anderson and Bass, 1986), or 40% (Duffy and Anderson, 1989; Duffy *et al.*, 1995) olivine. Thus, “pyrolite” and “piclogite” represent broad families of mantle compositions that are distinguished primarily by the former having >50% olivine by volume and the latter having <50% olivine.

Estimates of a suitable peridotite composition have also varied: from 40–70% olivine (Weidner, 1986), to 66–74% (Bina and Wood, 1987), to ~52% (Bina, 1993), for example. Indeed, for several years these two end-member models seemed to be converging towards 50% olivine (Ita and Stixrude, 1992; Jeanloz, 1995; Agee, 1998; Shearer and Flanagan, 1999). As the arguments hinge upon comparisons of seismic wave velocities in the upper mantle with velocity profiles computed for candidate mineral assemblages, firmer constraints upon this number require not only better experimental measurements of the simultaneous dependence of the elastic properties of mineral assemblages upon both temperature and pressure (Sinogeikin *et al.*, 1998; Zha *et al.*, 1998b) but also increased seismological resolution of the laterally varying velocity contrasts at depth within the upper mantle (Melbourne and Helmberger, 1998).

2.02.2.2 Velocity Contrasts

Seismology constrains these contrasts through observations of P - and S -wave travel times. Mathematical inversion of large numbers of travel times, observed at a variety of distances between source (earthquake) and receiver (seismometer), results in velocity profiles that represent the variation of V_P and V_S (or V_ϕ) as functions of depth. The increase in velocities across seismic “discontinuities” in these models can then be compared to the velocity changes across phase changes in olivine, as calculated from laboratory data, in order to estimate mantle olivine content. Unfortunately, seismic velocity profiles determined from such inversions generally are not very sensitive to, and therefore do not well constrain, the magnitudes of velocity discontinuities, and this is especially true of globally averaged seismic velocity models. Local or regional studies that include travel times of special seismic arrivals that have interacted directly with (reflected by or undergone P - S conversions at) the seismic discontinuities are best able to provide such constraints.

Measurements of elastic wave velocities in olivine and wadsleyite at high pressures and

temperatures (Li *et al.*, 2001) generate “remarkable consistency” between a standard pyrolite model containing ~60% olivine and high-resolution seismic velocity profiles of the transition zone. Arguments about $\pm 5\%$ olivine aside, we can perhaps safely refer to the upper mantle as a peridotite, as the IUGS classification of ultramafic rocks defines a peridotite as containing 40% or more olivine.

2.02.2.3 Discontinuity Topography

Perhaps one of the most important consequences of a peridotite composition for the upper mantle is that the phase transitions in olivine that are manifested as seismic discontinuities should exhibit thermally controlled variations in their depth of occurrence that are consistent with the measured Clapeyron slopes (Bina and Helffrich, 1994) of the transitions. In particular, the olivine–wadsleyite transition at 410 km should be deflected upwards in the cold environment of subduction zones while the disproportionation of ringwoodite to silicate perovskite and magnesiowüstite at 660 km should be deflected downwards, thereby locally thickening the transition zone. In anomalously warm regions (such as the environs of mantle plumes as described below), the opposite deflections at 410 and 660 should locally thin the transition zone. The seismically observed topography of 20–60 km on each of the 410 and 660 is consistent with lateral thermal anomalies of 700 K or less (Helffrich, 2000; Helffrich and Wood, 2001).

Other consequences of thermally perturbed phase relations in mantle peridotite (Figure 2) are also supported by seismological observations. These include anticorrelation of transition zone thickness and transition zone delay times, whereby positive delays in travel times, which imply slow velocities (and therefore high temperatures), are observed to correlate with negative changes in (thinning of) transition zone thickness (Gu and Dziewonski, 2002; Lebedev *et al.*, 2002).

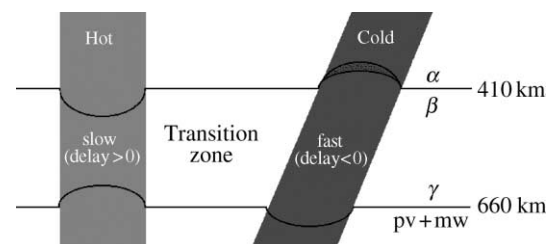


Figure 2 Schematic illustration of thermal control of olivine phase transformations in the transition zone, showing perturbations to transition zone thickness, transition zone seismic velocities (delay times), and depths of individual phase transformations.

Similarly, observations of anticorrelation of transition zone thickness and the depth to the 410 km discontinuity are consistent with thermal deflection of phase boundaries, as a positive increase in transition zone thickness (implying low temperatures) correlates with a negative change in depth to (implying uplift of) the 410 (Kind *et al.*, 2002). Furthermore, seismological observations suggest the presence of a thicker (colder) transition zone under continents than under (warmer) oceans (Gu and Dziewonski, 2002), as well as a thicker transition zone beneath (colder) subduction zones than beneath the (warmer) mid-Pacific (Gu and Dziewonski, 2002; Shearer *et al.*, 2002). Although evidence for the expected anticorrelation of topography on the 410 and the 660, whereby one may be expected to deflect upwards in any locale where the other deflects downwards, has been less robust than these other observations (Helffrich, 2000; Shearer *et al.*, 2002), such anticorrelation may be obscured by the dependence of absolute depth estimates upon assumptions about shallower velocity structures, as discussed later in the context of the depths of origin of mantle plumes. Clear anticorrelation of 410 and 660 topography may also be confounded by frequency-dependent effects (Helffrich and Bina, 1994; Helffrich, 2000): while the 660 may remain sharp in both cold and warm environments, the 410 should grow sharper in warm regions and more diffuse in cold regions, so that these two discontinuities may respond differently to seismic waves of different wavelengths at different temperatures. Overall, however, the bulk of the observational evidence indicates that topography on seismic discontinuities in the transition zone is caused by thermal perturbations of equilibrium phase transformations in a mantle of peridotite composition (Helffrich and Wood, 2001).

2.02.2.4 Sharpness

Other arguments about the composition of the transition zone have focused specifically upon the observed seismic “sharpness” or depth extent of the 410 km discontinuity, which sometimes appears to occur over a narrower depth interval than might be expected for the olivine–wadsleyite phase transition. A number of phenomena have been invoked to explain apparent variations in transition sharpness. These include kinetic effects on phase transformations (Solomatov and Stevenson, 1994), whereby low-pressure phases persist metastably for a finite extent before abruptly transforming to the stable high-pressure phases, thus eliminating what might otherwise be a finite mixed-phase regime. The probable nonlinearity of multivariant phase changes is another factor (Helffrich and Bina, 1994; Stixrude, 1997),

whereby a gradual transition appears seismically to be sharper because a large fraction of the associated velocity change is concentrated within a particular portion of the mixed-phase regime. Differential solubility of water within minerals across phase changes (Wood, 1995; Helffrich and Wood, 1996; Smyth and Frost, 2002) can also affect transition sharpness, in that small amounts of dissolved H₂O should broaden the $\alpha \rightarrow \beta$ transition at 410, while an excess of H₂O resulting in a free fluid phase may be expected to sharpen the same transition. Because the sharpness of the 410 may be particularly sensitive to water, some studies have begun to attempt to map water contents in the transition zone by examining the manner in which its sharpness appears to vary as a function of the frequency (and hence wavelength) of the interacting seismic waves (van der Meijde *et al.*, 2002).

Studies of multiphase Mg–Fe partitioning between coexisting olivine, wadsleyite, pyroxene, and garnet have also suggested that such partitioning can act to sharpen the $\alpha \rightarrow \beta$ transition at 410 (Irifune and Isshiki, 1998; Bina, 1998a). It is somewhat ironic that the nonolivine phases that exhibit a very broad pyroxene–garnet transition can, nonetheless, induce the already sharp olivine–wadsleyite transition to grow yet sharper simply by slightly shifting the effective Mg/Fe ratio in olivine through cation exchange.

2.02.2.5 Broadening and Bifurcation

As noted above, low temperatures alone can serve to broaden the 410 by expanding the depth extent of $\alpha + \beta$ mixed-phase stability field (Katsura and Ito, 1989; Bina and Helffrich, 1994). Even more confusingly, however, low temperatures can give rise to bifurcation of the $\alpha \rightarrow \beta$ transition (Figure 3), resulting in a strongly uplifted $\alpha \rightarrow \alpha + \gamma$ transition, which is seismically diffuse, overlying a less strongly uplifted $\alpha + \gamma \rightarrow \alpha + \beta$ or $\alpha + \gamma \rightarrow \beta + \gamma$ transition, which is seismically sharp (Green and Houston, 1995; Vacher *et al.*, 1999; Bina, 2002). As a result, α still transforms to β (and eventually to γ), but it does so by a two-step process, and whether a strongly uplifted broadened transition or a weakly uplifted sharpened transition is observed may depend upon the frequency of the interacting seismic waves. While understanding of such sharpening and broadening processes may be important for resolving fine details of the thermal structure of the transition zone, they would seem to have less bearing upon the overall bulk chemistry of the upper mantle, with the possible exception of constraints on local volatile contents (Wood *et al.*, 1996).

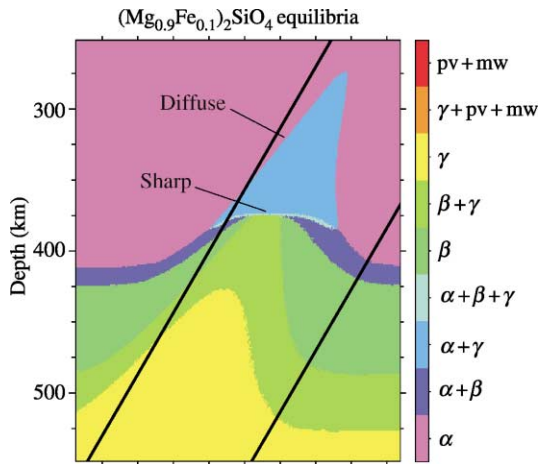


Figure 3 Effects upon olivine phase equilibria near 410 km depth of low temperatures in subduction zones, for mineral thermodynamic parameters of [Fei et al. \(1991\)](#). Dark lines denote boundaries of subducting slab. Phases are: (α) olivine, (β) wadsleyite, (γ) ringwoodite, (mw) magnesiowüstite, and (pv) ferromagnesian silicate perovskite. Note that the $\alpha \rightarrow \beta$ transition near 410 km is first uplifted and then bifurcates into a strongly uplifted diffuse $\alpha \rightarrow \alpha + \gamma$ transition overlying a weakly uplifted sharp boundary (after [Bina, 2002](#)) (vertical resolution is 1 km).

However, within the cold environment of subduction zones, the temperature dependence of phase relations in olivine near depths of 410 km does exhibit particular sensitivity to bulk $Mg/(Mg + Fe)$ ratios. Indeed, the effect on olivine phase relations of iron enrichment is largely analogous to that of lower temperatures noted above. For pyrolitic values ($Mg/(Mg + Fe) = 0.90$), equilibrium phase relations ([Fei et al., 1991](#)) predict uplift and broadening of the sharp $\alpha \rightarrow \beta$ transition in the cold slab, replacement of the sharp $\alpha \rightarrow \beta$ transition by a more diffuse $\alpha \rightarrow \alpha + \gamma$ transition overlying a sharper $\alpha + \gamma \rightarrow \alpha + \beta$ or $\alpha + \gamma \rightarrow \beta + \gamma$ transition within the colder interior of the slab, and uplift of the broad $\beta \rightarrow \beta + \gamma \rightarrow \gamma$ transition ([Figures 3 and 4](#)); this is equivalent to the bifurcated scenario discussed above for low temperatures. Further magnesium enrichment ($Mg/(Mg + Fe) = 0.99$) would result in smaller uplift of a sharper $\alpha \rightarrow \beta$ transition, little or no replacement of the sharp $\alpha \rightarrow \beta$ transition by a more diffuse $\alpha \rightarrow \alpha + \gamma$ transition within the cold interior of the slab, and an uplifted $\beta \rightarrow \gamma$ transition which is much sharper within both the slab and the ambient mantle; such sharpening is analogous to the effect of slightly warmer temperatures. This latter scenario would also correspond to a globally sharp 520 km discontinuity, as well as a globally sharp 410 km discontinuity which remains sharp when uplifted ([Figure 4](#)). However, iron enrichment ($Mg/(Mg + Fe) = 0.81$) would result

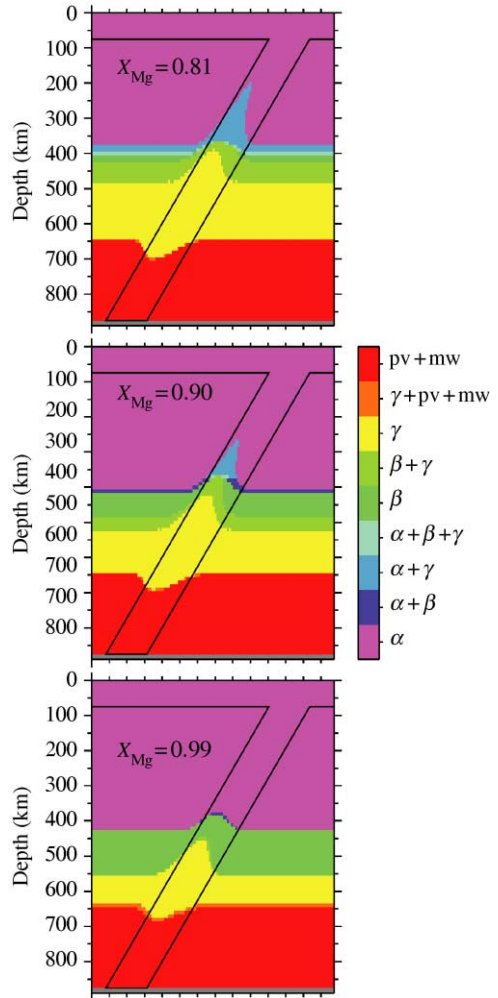


Figure 4 Effects upon olivine phase equilibria of variations in $Mg/(Mg + Fe)$ for pyrolite (center), Fe enrichment (top), and Mg enrichment (bottom) (vertical resolution is 10 km).

in complete replacement of the sharp $\alpha \rightarrow \beta$ transition within both the slab and the ambient mantle by a more diffuse and strongly uplifted $\alpha \rightarrow \alpha + \gamma$ transition overlying a sharper $\alpha + \gamma \rightarrow \alpha + \beta \rightarrow \beta$ or $\alpha + \gamma \rightarrow \beta + \gamma$ transition, as well as further broadening of the uplifted $\beta \rightarrow \beta + \gamma \rightarrow \gamma$ transition; this would be equivalent to the effect of very low temperatures. Such a scenario would correspond to a globally very diffuse 520 km discontinuity and a 410 km discontinuity consisting of a broad velocity gradient overlying a sharp velocity jump ([Figure 4](#)).

Other complexities of transition zone seismic structure may also indicate thermal or compositional effects. Apparent bifurcation of the 520 into superposed 500 km and 550 km discontinuities ([Deuss and Woodhouse, 2001](#)) may reflect distinct signatures of the $\beta \rightarrow \beta + \gamma \rightarrow \gamma$ transition and the exsolution of calcium silicate

perovskite from majoritic garnet (Figure 1), and the offset in depth between these two features may also be expected to change with temperature. Furthermore, in colder regions majoritic garnet may transform to silicate ilmenite (ilm) within the 550–600 km depth range, prior to eventual disproportionation to silicate perovskite and magnesiowüstite, but this interposed $gt \rightarrow ilm$ transition is unlikely to express a significant seismic velocity signature, at least not within subducting slabs (Vacher *et al.*, 1999). Overall, seismological observations of a sharp 410 km discontinuity—which is occasionally broader in places, exhibits some topography, and is accompanied by a sporadic 520 km discontinuity—are primarily consistent with pyrolitic $Mg/(Mg + Fe)$ values of 0.90, but local variations certainly cannot be excluded.

2.02.3 UPPER-MANTLE HETEROGENEITY

2.02.3.1 Subducted Basalts

The fate of the basalts and gabbros in the oceanic crust as they are subducted into a peridotite upper mantle (Chapter 2.03) can also be studied using seismological methods. Anhydrous metabasalts may be expected to undergo equilibrium transformation to an eclogite assemblage (with growth of garnet at the expense of plagioclase) around depths of 20–50 km (Wood, 1987; Peacock, 1993; Hacker, 1996). Such eclogites should be $\sim 2\%$ faster than surrounding pyrolite at depths of ~ 280 km (Helffrich *et al.*, 1989; Helffrich and Stein, 1993). However, most of this velocity contrast arises solely from the temperature contrast between cold slab (1,000 °C at 9.6 GPa) and warmer mantle, with the composition difference alone giving rise to a contrast of only $\sim 0.5\%$ (Helffrich *et al.*, 1989). Consideration of silica-oversaturated basalt compositions can expand this range of velocity contrasts somewhat, with anhydrous coesite eclogites being ~ 2 – 4% fast and, subsequent to the transition from coesite to stishovite at ~ 220 – 240 km depth, stishovite eclogites being ~ 4 – 6% fast (Connolly and Kerrick, 2002). Again, however, it is important to bear in mind that much of this contrast arises due to low slab temperatures alone, so that thermally equilibrated eclogites lingering long in the upper mantle would appear only slightly (if at all) fast relative to ambient mantle.

In large part, this ability of anhydrous basaltic eclogites to seismically blend into an ultramafic mantle arises from the behavior of elastic moduli in pyroxenes. In the shallowest upper mantle, orthopyroxene is $\sim 6\%$ slow in V_P relative to olivine and about equal in V_S . However, the bulk

modulus of orthopyroxene exhibits a strong and nonlinear increase with pressure, so that there is little significant difference in either V_P or V_S between orthopyroxene and olivine by ~ 200 km depth (Flesch *et al.*, 1998; James *et al.*, 2001). This absence of effective velocity contrasts between anhydrous eclogites and mantle peridotites within most of the upper mantle (Helffrich *et al.*, 1989; Helffrich, 1996) is also evident in the observation that model upper mantles of both pyrolite ($\sim 60\%$ olivine) and piclogite ($\sim 40\%$ olivine) composition exhibit similar velocities over the 100–400 km depth range (Vacher *et al.*, 1998).

If anhydrous metabasalts in an eclogite assemblage can generate only small fast velocity anomalies or no anomalies at all, then a puzzle emerges in understanding subduction zone structures. Seismological observations in Japan, Tonga, Alaska, and other active subduction zones demonstrate the presence of 4–10% slow velocities in a layer 2–10 km thick along the upper surfaces of subduction zones in the depth range 100–250 km (Helffrich, 1996; Connolly and Kerrick, 2002). One explanation that has been advanced to explain the presence of such low-velocity layers involves kinetic hindrance in cold slabs. Rather than equilibrium transformation of slow anhydrous gabbro to fast eclogite at depths of 20–50 km, a model of metastable persistence of gabbro into the blueschist and eclogite stability fields, perhaps below 100 km depth, has been invoked (Hacker, 1996; Connolly and Kerrick, 2002). However, it appears that this model of metastable anhydrous gabbro may not be appropriate (Helffrich, 1996), not only because oceanic basalts commonly are found to be hydrothermally altered but also because metastable gabbro appears to be too slow seismically (Connolly and Kerrick, 2002).

Indeed, hydrothermal alteration of basalts may be the key to understanding the low-velocity layers in subducting slabs. In hydrous metabasalts under subduction zone conditions, lawsonite blueschist is expected to be the initially dominant facies (Peacock, 1993). At 65 km depth in subducting basaltic crust, lawsonite blueschist would be $\sim 7\%$ slower than the overlying peridotite mantle and $\sim 8\%$ slower than the underlying garnet harzburgite layer of the subducting lithosphere, suggesting that hydrous metabasalts may be the cause of the seismologically detected low-velocity layers (Helffrich, 1996). As hydrous gabbroic crust subducts beyond the blueschist regime, the resulting equilibrium lawsonite eclogites should still be 3–7% slow (Connolly and Kerrick, 2002). With continued subduction, garnet increases and lawsonite decreases in abundance, until the coesite–stishovite transition near 220–240 km further

destabilizes lawsonite, giving rise to stishovite eclogites which should be 4–6% fast (Connolly and Kerrick, 2002). Such a change from slow lawsonite eclogites or coesite eclogites to fast stishovite eclogites is consistent with the observed termination of low-velocity layers and, indeed, with the occasional presence of high-velocity layers, below 250 km depth.

Interestingly, a dominant role for lawsonite eclogites in subducting oceanic crustal material may be echoed in the occurrence of lawsonite (or pseudomorphs thereafter) among the glaucophane eclogites of the Alpine Sesia zone, a complex of continental provenance presumably exhumed after subduction to at least 60 km depth (Reinsch, 1979; Pognante, 1989). Furthermore, the compositions of majoritic and sodium-rich garnets occasionally found as inclusions in diamonds (Chapter 2.05) are also consistent with equilibrium phase relations for basaltic crust which has penetrated into the transition zone (Ono and Yasuda, 1996). Within the transition zone, evidence from seismic tomography suggests that some subducting slab material penetrates directly into the lower mantle while, in other subduction zones, some is deflected horizontally at depths shallower than 1,000 km (Takenaka *et al.*, 1999; Fukao *et al.*, 2001). By the time subducted basaltic material enters the lower mantle, it should be largely dehydrated and should adopt a simpler, high-pressure perovskite mineralogy. The expected seismic signatures of such basaltic material in the lower mantle will be examined in a later section.

2.02.3.2 Plume Origins

While much attention has been focused upon the seismological properties of subduction zones, in part because of their significant spatial extent and associated mass flux (Chapter 2.11), seismological studies of hotspot areas are also illuminating, particularly with regard to ascertaining the depth of origin of plume structures. There are two primary types of seismic evidence for constraining the depth of origin of mantle plumes. The first of these consists of seismic tomographic imaging, in which one might expect the achievement of sufficiently fine spatial resolution for imaging narrow plume conduits to be a significant challenge. Indeed, this challenge is further aggravated by the fact that the resolution of such methods tends to decay within the crucial region of the mantle transition zone.

Nevertheless, seismic tomography has been employed in efforts to image the roots of mantle plumes (VanDecar *et al.*, 1995) and to determine whether or not they arise from deep-seated sources. An instructive example is the case of the Iceland hotspot, which tomographic images

suggest may be connected to a deep-seated plume source (Wolfe *et al.*, 1997). Such a conclusion is consistent with the fact that low seismic velocity anomalies appear to extend downward into the transition zone beneath the hotspot while they do not extend below 150 km beneath the rest of the mid-Atlantic ridge (Montagner and Ritsema, 2001), an observation supported by both global and regional tomography (Ritsema *et al.*, 1999; Allen *et al.*, 2002). However, this interpretation has been challenged. Foulger *et al.* (2001), claiming tomographic resolution to 450 km depth, conclude that the shape of the imaged low-velocity anomaly changes from cylindrical to tabular near the top of the transition zone, and the investigators argue on the basis of this apparent change in morphology that the plume does not extend to deeper levels. Alternatively, Allen *et al.* (2002), claiming resolution to 400 km depth, report a simple cylindrical morphology at depth. Detailed numerical tests of the spatial resolution of tomographic imaging under Iceland (Keller *et al.*, 2000) suggest that a deep-seated plume may not be required to explain the observed seismic delay times. In a similar vein, Christiansen *et al.* (2002) argue that there is a dearth of convincing seismic evidence for a plume extending to depths below 240 km beneath the Yellowstone hotspot. All of this serves to highlight some of the persistent ambiguities present in interpretation of seismic tomographic images beneath hotspots, images which remain nonunique results of the application of a variety of optimization functions to different observational data sets.

The second type of seismic evidence used to constrain the depth of origin of mantle plumes consists of analyses of boundary-interaction phases. Such phases consist of seismic waves which, by interacting with the boundaries generally known as seismic “discontinuities,” have undergone conversion (repartitioning of energy between longitudinal (*P*) and transverse (*S*) waves) and/or reflection (repartitioning of energy between upgoing and downgoing waves). For the purposes of studying mantle plumes, the crucial measurements are differential travel times between those phases which interact with the 410 discontinuity and those which interact with the 660 discontinuity. Such differential times translate (via a reference velocity model) into measures of the thickness (depth extent) of the transition zone lying between these two discontinuities.

Given the opposing signs of the Clapeyron slopes of the primary phase transitions associated with these seismic discontinuities, any elevated mantle temperatures associated with thermal plumes may be expected to yield thinning of the transition zone (Figure 2), via depression of the 410 and uplift of 660 (Shen *et al.*, 1998; Bina, 1998c; Lebedev *et al.*, 2002). Some global and

broad regional studies (Vinnik *et al.*, 1997; Chevrot *et al.*, 1999) have detected no clear correlation between such estimates of transition zone thickness and locations of hotspots (Keller *et al.*, 2000). Since the late 1990s, however, a number of more localized studies have measured transition zone thinning of several tens of kilometers, suggesting hot thermal anomalies of a few hundred degrees, over regions with diameters of hundreds of kilometers, beneath such presumed thermal plume features as the Snake River plain (Dueker and Sheehan, 1997), Iceland (Shen *et al.*, 1998), Yellowstone (Humphreys *et al.*, 2000), Hawaii (Li *et al.*, 2000), and the Society hotspot (Niu *et al.*, 2002). By contrast, no apparent thinning has been found beneath tectonically inactive areas such as the northern North Sea (Helfrich *et al.*, 2003). A straightforward interpretation of these results is that the transition zone beneath plumes is hotter than “normal” mantle, with thermal plumes originating either deep in the lower mantle below the transition zone or (at the shallowest) in a hot thermal boundary layer at the base of the transition zone.

The picture grows less simple, however, if we attempt to inquire into how the causes of this transition zone thinning are distributed between 410 and 660. Such inquiry involves estimating the actual absolute depths of these two seismic discontinuities beneath plumes. While the use of differential times to estimate thickness requires a reference velocity model within the transition zone, the use of absolute times to estimate individual depths further requires a (laterally varying) reference velocity model from the transition zone all the way up to the surface. A simple model of a deep-seated thermal plume suggests that we should observe a depressed 410 with an uplifted 660, which is what seems to be imaged beneath Iceland (Shen *et al.*, 1998). However, we can also find a flat 410 with an uplifted 660 beneath Hawaii (Li *et al.*, 2000), a weakly uplifted 410 with a strongly uplifted 660 beneath the Snake River plain (Dueker and Sheehan, 1997) and Yellowstone (Humphreys *et al.*, 2000; Christiansen *et al.*, 2002), or a depressed 410 with a flat 660 beneath the Society hotspot (Niu *et al.*, 2002). Taken at face value, a depressed (hot) 410 with an uplifted (hot) 660 suggests a plume origin in the lower mantle (Shen *et al.*, 1998). A flat (normal) 410 with an uplifted (hot) 660 suggests either an origin in the lower mantle (Li *et al.*, 2000) or the presence of a thermal boundary layer within the transition zone, as does an uplifted (cold) 410 with an uplifted (hot) 660. A depressed (hot) 410 with a flat (normal) 660 suggests an origin within the transition zone (Shen *et al.*, 1998). Interestingly, the one combination which would strongly suggest an origin within the shallow upper-mantle,

a depressed (hot) 410 with a depressed (cold) 660, is not observed. It is complexities such as these that have led several investigators to argue against the idea of deep-seated plumes in favor of the dominance of upper-mantle processes in the origins of hotspots (Anderson, 1994, 2001; Saltzer and Humphreys, 1997; Christiansen *et al.*, 2002), including such detailed proposals as “propagating convective rolls organized by the sense of shear across the asthenosphere” (Humphreys *et al.*, 2000). This latter proposal would explain a cold 410 overlying a hot 660 (and underlying another hot region near 200 km depth), e.g., through localized convection at depths shallower than 400 km (Humphreys *et al.*, 2000).

There are a range of other possible explanations for these seeming complexities, however, a primary factor being the aforementioned reliance of absolute depth estimates for seismic discontinuities upon accurate models of shallow velocity structures (Walck, 1984; Helfrich, 2000; Niu *et al.*, 2002). If absolute depth estimates are so sensitive to assumptions about shallower structures, then these various and seemingly paradoxical combinations of apparent deflections may arise simply from inaccurate representations of structure outside of the regions of study. Conclusions drawn from differential times, which are free of such dependence upon assumptions about distal regions, may be judged more robust. Such a stance also renders more tractable an understanding of the magnitudes of the implied thermal anomalies. If all of the observed thinning of the transition zone were caused by deflection of either the 410 or 660 alone, then hot temperature anomalies of ~ 400 K would be required, but the size of the requirement falls to ~ 200 K if the thinning is shared between anticorrelated 410 and 660 deflections (Helfrich, 2000; Niu *et al.*, 2002).

Another factor to consider is an inherent seismological bias toward underestimating topography. For example, the “Fresnel zones” that describe the regions of the discontinuities that are sampled by boundary-interaction phases can be both large in extent and irregular in shape (Helfrich, 2000; Niu *et al.*, 2002), so that the measured travel times incorporate entwined interactions with both deflected and undeflected portions of a given discontinuity. Moreover, such seismological biases can yield greater underestimates of topography at 410 than at 660 (Neele *et al.*, 1997; Helfrich, 2000), which is consistent with the apparent “cold 410” puzzle noted above. Indeed, some topography simply may not be clearly visible. While the $\alpha \rightarrow \alpha + \beta \rightarrow \beta$ transition should grow sharper at high temperatures as well as being depressed, any small-scale topography on or “roughening” of discontinuity surfaces can render undetectable the very P -to- S conversions which indicate the presence of

topography (van der Lee *et al.*, 1994; Helffrich *et al.*, 2003). Again, such effects may be more significant near 410, where the magnitudes of Clapeyron slopes and hence of topography may be larger (Bina and Helffrich, 1994), but they may also be significant near 660 (van der Lee *et al.*, 1994). Furthermore, the apparent magnitude of discontinuity topography will vary with the frequency of the seismic waves used to probe it (Helffrich, 2000).

Finally, there is yet another possible contributor to the apparent “cold 660” puzzle noted above. It is the negative Clapeyron slope of the $\gamma \rightarrow \text{pv} + \text{mw}$ transition that predicts uplift of the 660 in hot plumes. The $\gamma \rightarrow \text{pv} + \text{mw}$ transition, however, may be replaced by a $\beta \rightarrow \text{pv} + \text{mw}$ transition at high temperatures, the latter exhibiting a positive Clapeyron slope and so allowing 660 depression instead of uplift (Liu, 1994). However, $\beta \rightarrow \text{pv} + \text{mw}$ appears to succeed $\gamma \rightarrow \text{pv} + \text{mw}$ only in pure Mg_2SiO_4 compositions, so this particular mechanism is unlikely to operate in real multicomponent mantle compositions (Bina and Liu, 1995; Niu *et al.*, 2002).

The primary point of this discussion, then, is that estimates of lateral variations in transition zone thicknesses from differential seismic travel times are more robust than estimates of lateral variations in the absolute depths of discontinuities from absolute travel times. There are many factors, largely unrelated to plumes, that may cause some underestimation of the former but which induce serious complications in the latter. Certainly, it is possible that the overall tectonic system, including some hotspot-designated volcanic chains, may be controlled to a significant extent from above via the lithosphere rather than from below via the deep mantle (Anderson, 2001). However, the simplest interpretations consistent with observations of transition zone thinning, despite some apparent inconsistencies in estimates of absolute depths of discontinuities, strongly suggest that some hotspots are associated with plume-like thermal anomalies that penetrate the transition zone. Given the great disparities in heat and mass flux among different hotspots, however, there is certainly room for diversity in the family of thermal plumes, and it would not be surprising ultimately to discover various classes of plumes associated with different depths of origin (Kerr, 2003).

2.02.4 LOWER-MANTLE BULK COMPOSITION

2.02.4.1 Bulk Fitting

Given that the properties of the 660 km seismic discontinuity are in excellent agreement with

the predicted behavior of an isochemical phase transformation, it might seem reasonable to assume that the lower mantle below this depth possesses largely the same bulk composition as the upper mantle above. This assumption has been regularly challenged, however, based largely upon cosmochemical concerns (Anderson, 1989; Bina, 1998b), upon estimates of mass fluxes between geochemical reservoirs (Helffrich and Wood, 2001), or upon driving forces for chemical differentiation across phase transitions (Garlick, 1969; Kumazawa *et al.*, 1974; Walker and Agee, 1989; Bina and Kumazawa, 1993; Liu and Ågren, 1995). Concern has focused primarily upon whether the lower mantle might be enriched in iron and/or silicon relative to the upper mantle.

A simple way to address this question is to compute profiles of density and bulk sound velocity (thereby avoiding the large uncertainties associated with extrapolating shear moduli), along plausible lower-mantle adiabats, for a variety of candidate lower-mantle compositions and to compare these model profiles to a reference seismological model such as *ak135* (Kennett *et al.*, 1995). Examination of the r.m.s. misfit between such models over the entire lower mantle quickly reveals several important principles. Density (Figure 5) is primarily sensitive to $\text{Mg}/(\text{Mg} + \text{Fe})$ but not to silica content. Velocity (Figure 5) sensitivity, alternatively, exhibits a trade-off between $\text{Mg}/(\text{Mg} + \text{Fe})$ and $\text{Si}/(\text{Mg} + \text{Fe})$. This suborthogonal nature of density and velocity sensitivities allows the two together (Figures 5 and 6) to constrain lower-mantle composition via the intersection of their respective misfit minima. The resulting family of allowable lower-mantle bulk compositions (Figure 6) includes a pyrolite mantle composition. While some uncertainty in silicon content remains, there is no evidence for iron enrichment of the lower mantle (Figure 6). The extent to which silicon enrichment of the lower mantle can be accommodated by the seismological constraints increases as the assumed temperature (at the root of the adiabat) of the lower mantle is increased (Figure 7). These schematic results are for a simple lower mantle mineralogy limited to ferromagnesian silicate perovskite (Fiquet *et al.*, 2000), magnesiowüstite (Fei *et al.*, 1992), and stishovite (Li *et al.*, 1996). Effects of other components (e.g., calcium, aluminum, sodium) have been neglected, and a depth-varying Mg–Fe partitioning coefficient between perovskite and magnesiowüstite (Mao *et al.*, 1997) has been employed. However, repetition of these analyses with the inclusion of calcium-silicate perovskite (Wang *et al.*, 1996) or the use of a depth-invariant partitioning coefficient (Kesson *et al.*, 1998) results in only very minor perturbations.

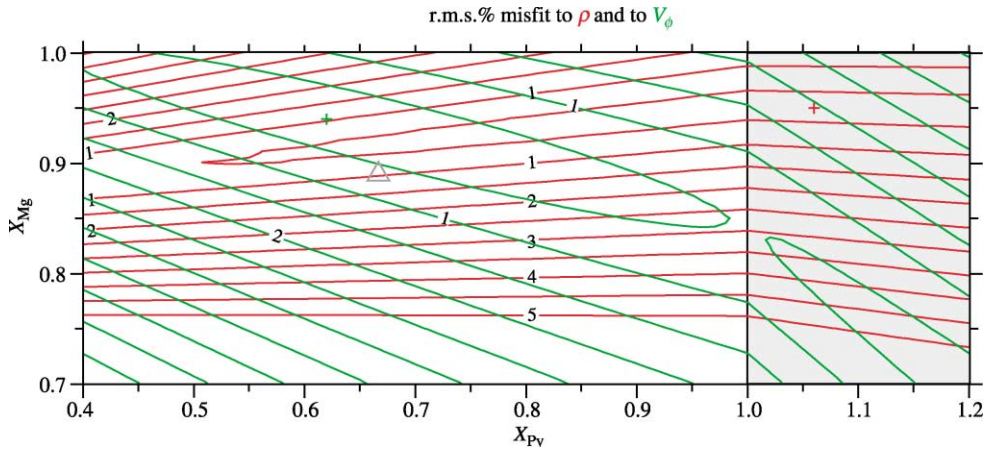


Figure 5 Contours of r.m.s misfit (%) to seismological reference model *ak135* of density (red) and bulk sound velocity (green) for candidate lower-mantle compositions, parametrized in terms of $\text{Mg}/(\text{Mg} + \text{Fe}) (= X_{\text{Mg}})$ and $\text{Si}/(\text{Mg} + \text{Fe}) (= X_{\text{Pv}})$, over the entirety of the lower mantle. Shaded region at $X_{\text{Pv}} > 1$ indicates free silica. Triangle denotes pyrolite. Plus signs denote minima of r.m.s. misfit. Root of lower-mantle adiabat is 2,000 K at 660 km depth.

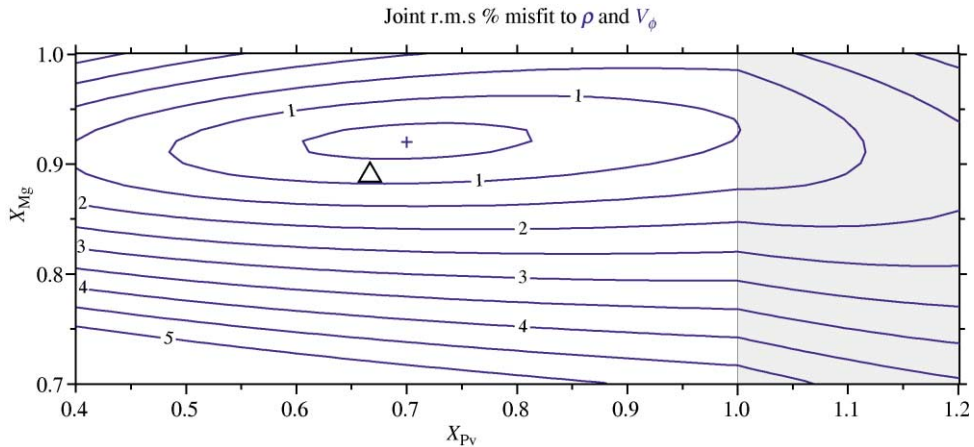


Figure 6 Contours of joint (blue) r.m.s. misfit (%) to seismological reference model *ak135* of density and bulk sound velocity for candidate lower-mantle compositions, parametrized in terms of $\text{Mg}/(\text{Mg} + \text{Fe}) (= X_{\text{Mg}})$ and $\text{Si}/(\text{Mg} + \text{Fe}) (= X_{\text{Pv}})$, over the entirety of the lower mantle. Shaded region at $X_{\text{Pv}} > 1$ indicates free silica. Triangle denotes pyrolite. Plus sign denotes minimum of r.m.s. misfit. Root of lower-mantle adiabat is 2,000 K at 660 km depth.

2.02.4.2 Depthwise Fitting

A different way of examining these relationships is to plot the best-fitting lower-mantle compositions within 10 km thick depth slices. Again, it is apparent (Figure 8) that density constrains only $\text{Mg}/(\text{Mg} + \text{Fe})$ while both density and velocity together are required to constrain $\text{Si}/(\text{Mg} + \text{Fe})$. Bulk sound velocity alone, as shown by the unstable oscillations in best-fitting compositions (Figure 8), does not effectively constrain either compositional parameter within such small depth slices. Throughout the bulk of the lower mantle, there is no evidence for iron enrichment, and the deviation from a pyrolite composition, in terms of both $\text{Mg}/(\text{Mg} + \text{Fe})$ and

$\text{Si}/(\text{Mg} + \text{Fe})$, falls within the overall 1% r.m.s. misfit contour (Figure 7). Indeed, the only statistically significant deviations of the best-fitting composition from pyrolite occur in the top ~ 300 km of the lower mantle and in the bottom ~ 200 km. For the former region, this deviation is not surprising, as we probably have not fully incorporated the appropriate mineralogy. While the $\gamma \rightarrow \text{pv} + \text{mw}$ transition in the olivine component occurs at 660 km depth, the attendant $\text{gt} \rightarrow \text{pv}$ transition in the majorite component may not achieve completion until 100 km deeper or more, due to the solubility of aluminum and ferric iron in both garnet–majorite and silicate perovskite (Wood and Rubie, 1996; McCammon, 1997). Thus, the anomalous best-fitting compositions in

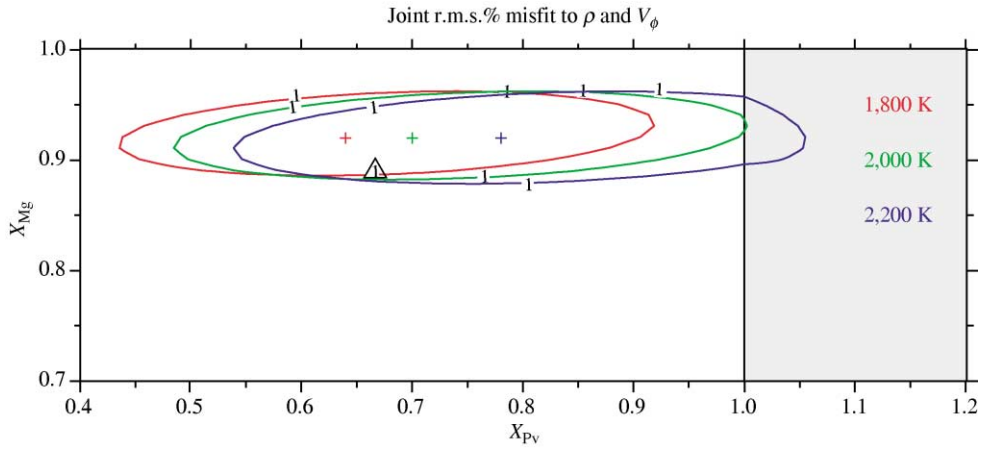


Figure 7 Contours of joint r.m.s. misfit (1%) to seismological reference model *ak135* of density and bulk sound velocity for candidate lower-mantle compositions, parametrized in terms of $\text{Mg}/(\text{Mg} + \text{Fe}) (= X_{\text{Mg}})$ and $\text{Si}/(\text{Mg} + \text{Fe}) (= X_{\text{Pv}})$, over the entirety of the lower mantle. Shaded region at $X_{\text{Pv}} > 1$ indicates free silica. Triangle denotes pyrolite. Plus signs denote minima of r.m.s. misfit. Roots of lower-mantle adiabats are 1,800 K (red), 2,000 K (green), and 2,200 K (blue) at 660 km depth.

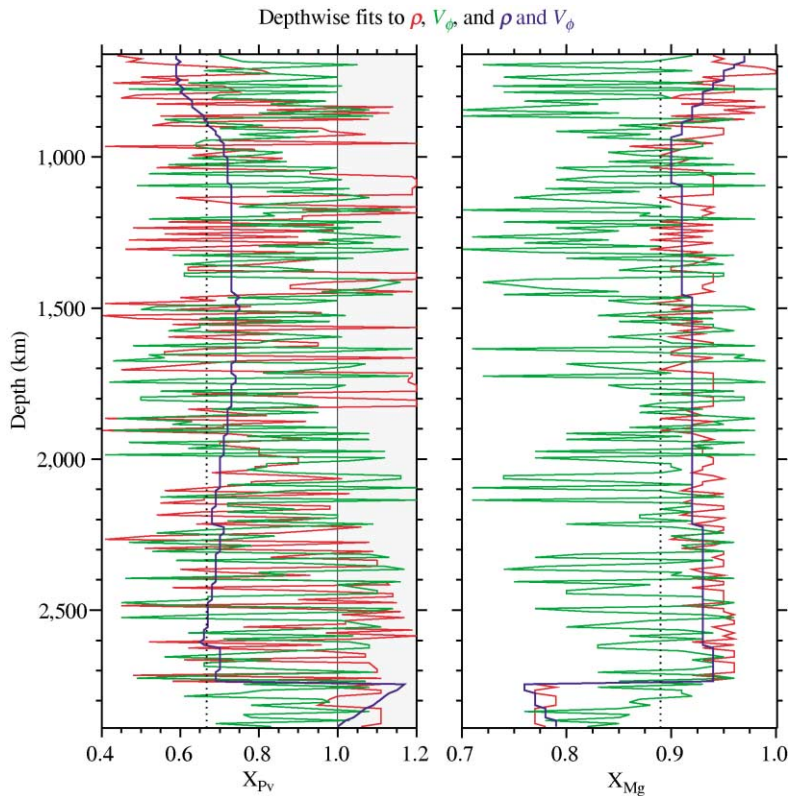


Figure 8 Depthwise best-fit compositions to seismological reference model *ak135* for density alone (red), bulk sound velocity alone (green), and both density and bulk sound velocity jointly (blue), with compositions parametrized in terms of $\text{Mg}/(\text{Mg} + \text{Fe}) (X_{\text{Mg}})$ and $\text{Si}/(\text{Mg} + \text{Fe}) (X_{\text{Pv}})$, in 10 km depth slices through the lower mantle. Shaded region at $X_{\text{Pv}} > 1$ indicates free silica. Dotted lines (at $X_{\text{Pv}} = 0.67$ and $X_{\text{Mg}} = 0.89$) denote pyrolite. Root of lower-mantle adiabat is 2,000 K at 660 km depth.

the top 200–300 km of the lower mantle probably arise simply from our omission of garnet from the model mineralogy. The situation in the bottom ~200 km of the lower mantle is more intriguing. Certainly, extrapolation of mineral properties are most uncertain in this region, and a globally averaged seismological model such as *ak135* may not accurately reflect details of structure near the core–mantle boundary. However, it is interesting to note that the implied iron enrichment and presence of free silica (Figures 8 and 9) are not inconsistent with what one might expect from interactions between silicate lower mantle and metallic core or from accumulation of subducted basaltic material at the core–mantle boundary.

Aside from the core–mantle boundary region, a pyrolite lower-mantle composition appears to be consistent with seismological constraints. Silica enrichment of the lower mantle can be accommodated if the lower mantle is hotter than expected for a simple adiabat rooted at the 660 km $\gamma \rightarrow \text{pv} + \text{mw}$ transition (Figure 9). Because any chemical boundary layer between the upper and lower mantle would be accompanied by a corresponding thermal boundary layer, such a model

of a chemically distinct and hot lower mantle is also internally consistent. This trade-off has been evident for decades (Birch, 1952; Jackson, 1983, 1998; Jeanloz and Knittle, 1989; Bina and Silver, 1990, 1997; Stixrude *et al.*, 1992; Zhao and Anderson, 1994). However, the seismological evidence (discussed above) that the transition zone capping the lower mantle behaves like a set of thermally governed isochemical phase transformations, coupled with the absence of seismic evidence (e.g., a globally sharp seismic reflector displaying hundreds of kilometers of dynamically induced topographic undulations) for a chemical boundary in the lower mantle, lends considerable support to the minimalist assumption that the bulk composition of the lower mantle greatly resembles that of upper-mantle peridotite.

2.02.5 LOWER-MANTLE HETEROGENEITY

2.02.5.1 Overview

Seismic velocity heterogeneity in the mantle, e.g., as revealed by seismic tomography, is often

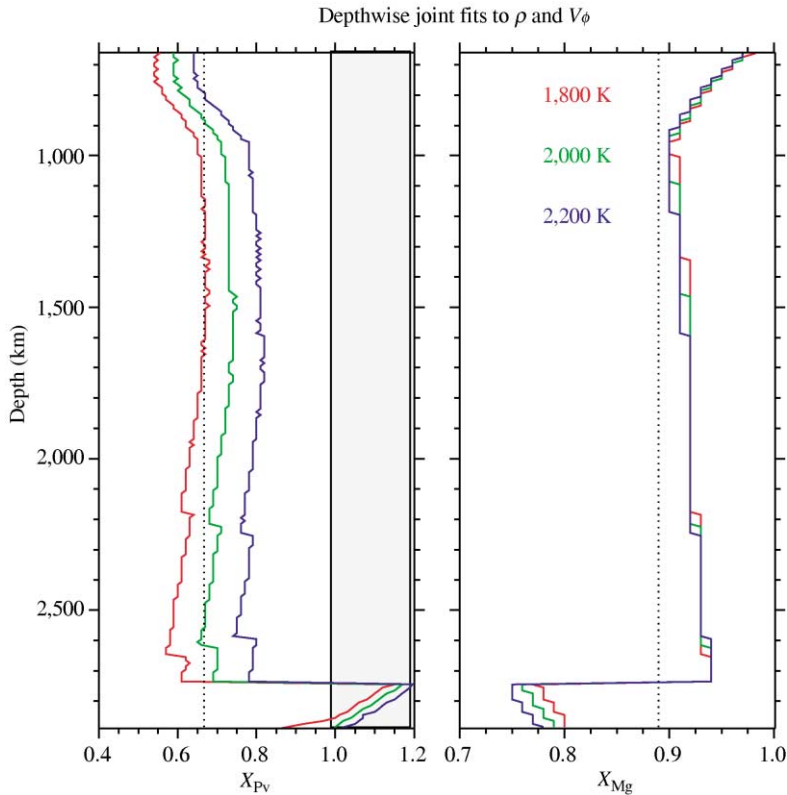


Figure 9 Depthwise best-fit compositions to seismological reference model *ak135* for both density and bulk sound velocity jointly, with compositions parametrized in terms of $\text{Mg}/(\text{Mg} + \text{Fe})$ (X_{Mg}) and $\text{Si}/(\text{Mg} + \text{Fe})$ (X_{Pv}), in 10 km depth slices through the lower mantle. Shaded region at $X_{\text{Pv}} > 1$ indicates free silica. Dotted lines (at $X_{\text{Pv}} = 0.67$ and $X_{\text{Mg}} = 0.89$) denote pyrolite. Roots of lower-mantle adiabats are 1,800 K (red), 2,000 K (green), and 2,200 K (blue) at 660 km depth.

interpreted in terms of strictly thermal origins. However, lateral variations in seismic velocity within the lower mantle (Hedlin *et al.*, 1997; Niu and Kawakatsu, 1997; Castle and Creager, 1999; Deuss and Woodhouse, 2002) may arise from a number of sources, including temperature anomalies (δT), local phase changes (δX_ϕ), and chemical heterogeneity (δX_i), and they should be accompanied by associated density anomalies. Thus, lower-mantle seismic velocity anomalies may reflect local heterogeneity in chemical composition, such as variations in iron–magnesium ratio and silica content, rather than simply variations in temperature. Together, thermal and chemical variations may jointly explain the manner in which the r.m.s. amplitudes of seismic velocity anomalies appear to vary with depth (Bina and Wood, 2000). The distinction is important because velocity anomalies arising from compositional differences are not subject to the same temporal decay as those due to thermal perturbations, due to different timescales for chemical diffusion and thermal conduction.

Temperature anomalies may arise due to low temperatures within cold subducted slab material, but such thermal anomalies will decay with time (and hence depth of penetration into the mantle) as the slab is thermally assimilated into the warmer mantle. Local phase changes are unlikely to occur on significant scales below transition zone depths, except perhaps in exotic compositions containing free oxides (Bina, 1998b). Chemical heterogeneity thus seems a reasonable candidate as a source of seismic velocity heterogeneity in the lower mantle, and an obvious source of major-element chemical heterogeneity is subducted slab material that retains the chemical differentiation acquired during its formation at spreading ridges.

2.02.5.2 Subducted Oceanic Crust

Formation of oceanic lithosphere involves chemical differentiation (by partial melting) of mantle lherzolite parent material (see Chapter 2.03 and Chapter 2.08). The complex structure of oceanic lithosphere closely approximates a simple model of a basaltic–gabbroic crustal layer overlying a depleted harzburgite layer, which in turn overlies lherzolitic peridotite mantle material. During subduction, these layers undergo phase transformations to denser phase assemblages with increasing depth of penetration into the mantle. For example, the basalt and gabbro components progressively transform to eclogite in the upper mantle, to garnetite in the transition zone, and to perovskitite in the lower mantle (Vacher *et al.*, 1998; Kesson *et al.*, 1998; Hirose *et al.*, 1999). Upon deep subduction, all of the components of a petrologically layered slab should transform to a

lower-mantle mineralogy, consisting of some subset of the phases (Mg, Fe, Al)SiO₃ ferromagnesian silicate perovskite, (Fe, Mg)O magnesiowüstite, CaSiO₃ calcium silicate perovskite, and SiO₂ stishovite, along with minor amounts of sodium-bearing and other phases. The seismic velocities and densities of these layers will differ due, e.g., to the coupled effects of silicon enrichment and magnesium depletion of the basaltic melt relative to the parent mantle.

Let us represent a subducting slab using a simple three-layered slab model (Helffrich and Stein, 1993), consisting of a basaltic crustal layer overlying a harzburgite layer overlying lherzolite mantle material. To represent the range of possible compositions of the basaltic crustal layer, we test both the “eclogite” of Helffrich *et al.* (1989) and the “gabbro” of Helffrich and Stein (1993), the latter being significantly richer in silicon and magnesium (Table 1). For the harzburgite layer, we adopt the “harzburgite” composition of Helffrich *et al.* (1989). For the mantle layer, we test both the “lherzolite” of Helffrich *et al.* (1989) and the “peridotite” of Helffrich and Stein (1993), the latter being slightly richer in silicon and iron (Table 1). We transform each of these bulk compositions into its stoichiometrically equivalent lower-mantle mineralogy (Table 2).

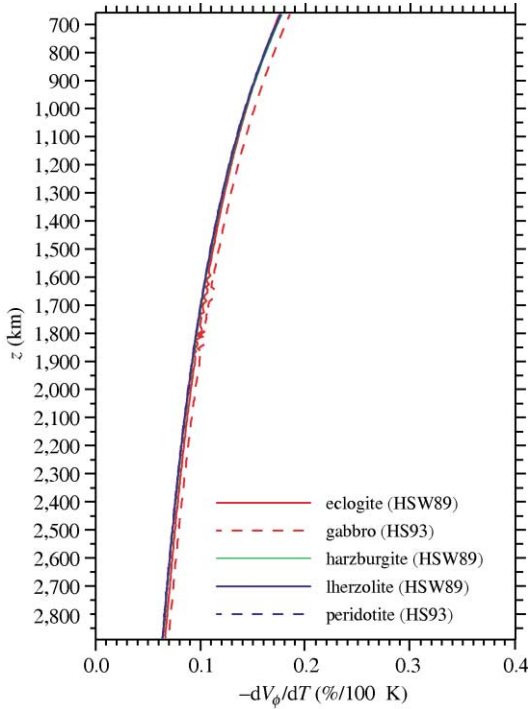
To isolate compositional and thermal effects, we calculate elastic properties for the various bulk compositions along adiabats rooted at a temperature of 2,000 K at 665 km depth (Bina, 1998b), using equations of state for (Mg, Fe)SiO₃ perovskite (Fiquet *et al.*, 2000), (Fe, Mg)O magnesiowüstite (Fei *et al.*, 1992), CaSiO₃ perovskite (Wang *et al.*, 1996), and SiO₂ stishovite (Li *et al.*, 1996; Liu *et al.*, 1996). We calculate Voigt–Reuss–Hill-averaged bulk sound velocities, to avoid the large uncertainties associated with extrapolating shear moduli to lower-mantle conditions. In these simple calculations, we have neglected the role of Al₂O₃ in silicate perovskite (Wood and Rubie, 1996; Wood, 2000), but the effects of this component upon the elastic properties—depressed bulk moduli (Zhang and Weidner, 1999)—are expected to be important only in the shallowest part of the lower mantle (Brodholt, 2000). Furthermore, we have assumed that any free silica is present as stishovite, rather

Table 1 Molar bulk compositions for model slab components.

	$Mg/(Mg + Fe)$	$Si/(Mg + Fe)$
Eclogite	0.57	1.65
Gabbro	0.64	2.58
Harzburgite	0.92	0.66
Lherzolite	0.90	0.68
Peridotite	0.89	0.69

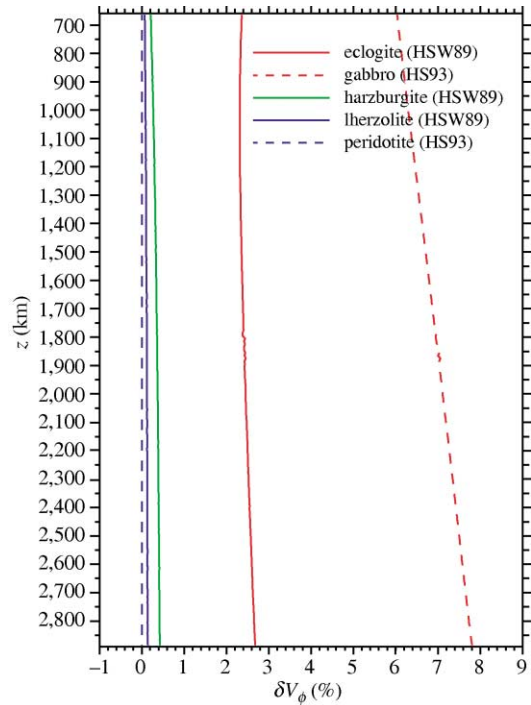
Table 2 Molar quantities at 665 km depth for model slab components.

	$pv\text{-MgSiO}_3$	$pv\text{-FeSiO}_3$	$mw\text{-MgO}$	$mw\text{-FeO}$	$st\text{-SiO}_2$
Eclogite	0.57	0.43	0.00	0.00	0.65
Gabbro	0.64	0.36	0.00	0.00	1.58
Harzburgite	0.63	0.03	0.29	0.05	0.00
Lherzolite	0.64	0.04	0.26	0.06	0.00
Peridotite	0.65	0.04	0.24	0.07	0.00

**Figure 10** Temperature dependence of the bulk sound velocity versus depth in the lower mantle, for candidate bulk compositions for the basaltic layer (red), the underlying harzburgite layer (green), and the basal lherzolite (blue). Note that temperature sensitivity falls with increasing depth.

than as higher-pressure SiO_2 polymorphs such as those with CaCl_2 and $\alpha\text{-PbO}_2$ structures (Karki *et al.*, 1997), so that our calculated velocities for the silica-oversaturated basaltic crustal components will represent conservative lower bounds.

The temperature dependence of the bulk sound velocity ($\partial V/\partial T$) for all of the compositions in the layered slab falls from below 0.2% per 100 K at the top of the lower mantle to below 0.1% per 100 K at the base of the lower mantle (Figure 10). As the magnitude of thermal anomalies associated with cold slab material will also fall with increasing depth as slabs thermally assimilate, this behavior suggests that it will be difficult to explain any large velocity anomalies at depth in terms of temperature alone. Indeed, even if thermal anomalies ~ 100 K were to somehow survive down to the base of

**Figure 11** Bulk sound velocity anomalies relative to peridotite mantle versus depth in the lower mantle (blue); for candidate bulk compositions for the basaltic layer (red) and the underlying harzburgite layer (green). Note that the basaltic layer is fast and grows faster with increasing depth.

the lower mantle, they would only give rise to velocity anomalies $\sim 0.1\%$.

Alternatively, the composition dependence of bulk sound velocity ($\partial V/\partial X_i$) is significantly greater (Figure 11), and bulk chemical anomalies should not change significantly with depth. The velocities for the two representative models of the underlying mantle layer, the “lherzolite” (Helffrich *et al.*, 1989) and “peridotite” (Helffrich and Stein, 1993) compositions, are virtually identical. Relative to the “peridotite” composition, the “harzburgite” (Helffrich *et al.*, 1989) layer is less than 0.5% fast. However, the basaltic crustal compositions yield significantly fast velocity anomalies, and anomaly magnitudes increase with depth. The “eclogite” (Helffrich *et al.*, 1989) rises from below 2.4% fast near 660 km

depth to above 2.6% fast near 2,890 km depth, and the more silica-rich “gabbro” (Helffrich and Stein, 1993) rises from $\sim 7.0\%$ fast to $\sim 7.8\%$ fast. Hence, it should be easier to generate large velocity anomalies through compositional variations, such as those associated with subducted slabs.

Thus, for temperature effects only, velocity anomalies should be small and decay with increasing depth. This effect would occur even for depth-invariant temperature anomalies, but it will be even more pronounced in the case of cold subducting material whose temperature anomalies should decay with increasing depth due to thermal assimilation. Even for large temperature anomalies, in the range of hundreds of degrees, velocity anomalies remain below 1%. For compositional effects, however, velocity anomalies due to chemical contrasts between basaltic/gabbroic material and peridotitic mantle should be large and grow with increasing depth. Such velocity anomalies should fall in the range 2–8% or greater.

Similar results have been reported by Mattern *et al.* (2002), using more recent equations of state for lower-mantle minerals and incorporating the solubility of alumina in silicate perovskite. They also used a three-layered slab model (mid-ocean ridge basalt (MORB) over harzburgite over pyrolite), but with a MORB composition ($\text{Si}/(\text{Mg} + \text{Fe}) = 2.29$) intermediate between our extreme end-members of the Helffrich *et al.* (1989) “eclogite” (1.65) and the Helffrich and Stein (1993) “gabbro” (2.58).

The high velocities in the basaltic material arise largely from the presence of free silica. As we have assumed that all free silica is in the form of stishovite, rather than as higher-pressure SiO_2 polymorphs, actual lower-mantle velocity perturbations arising from basaltic crustal material may be even larger than the values calculated here. Free silica in the former crustal material, however, should react with magnesiowüstite in the surrounding lower-mantle material to form silicate perovskite. Thus, survival of free silica in the lower mantle may require formation of perovskite rinds to preserve the free silica from reaction with magnesiowüstite, just as porphyroblasts can protect inclusions (which would otherwise become reactants) to form “armored relics” in more familiar metamorphic rocks.

Damping and smearing arising from regularization in seismic tomography typically cause narrow, intense anomalies to be imaged as broader, more subdued anomalies (Garnero, 2000). Thus, layers of basaltic/gabbroic material ~ 10 km thick that are $\sim 5\%$ fast, e.g., might perhaps appear as $\sim 0.5\%$ velocity anomalies distributed over 100 km thick slabs. If this is the case, then one might seek frequency-dependent

effects in seismological observations, in which the apparent magnitude of velocity anomalies rises with the spatial resolving power of the seismic probe. Studies of lower-mantle seismic scatterers have suggested that bodies of 100 km or less in size exhibit velocity anomalies of several percent (Kaneshima and Helffrich, 1998; Garnero, 2000), especially near subduction zones. Some studies find evidence of 0.8–2.0% lower-mantle *P*-wave velocity heterogeneities at length scales of less than 8 km (Hedlin *et al.*, 1997), as well as lower-mantle *S*-wave velocity structures that are either $>4\%$ slow and ~ 8 km thick or $>8\%$ fast (Kaneshima and Helffrich, 1999). Such narrow but fast velocity anomalies are consistent with our model of lower-mantle velocity anomalies in subducted oceanic lithosphere.

Of course, we have calculated only bulk sound velocities here. Detailed comparison with seismological observations will require computation of *P*- and *S*-wave velocities, which in turn must await better constraints on the pressure and temperature dependence of the shear moduli of lower-mantle mineral phases. Furthermore, the velocity perturbations that we have calculated to arise from thermal and compositional anomalies will be accompanied by associated density anomalies. While the harzburgite is $\sim 1\%$ less dense than mantle peridotite, basaltic crustal material should be 1–7% denser than peridotite under lower-mantle conditions (Figure 12). The magnitude of this latter density anomaly should fall with increasing depth (Figure 12), as should the density consequences of thermal anomalies (Figure 13). These extrapolations suggest that metagabbros should remain denser than peridotite throughout the lower mantle, as do others which additionally incorporate the affects of calcium and aluminum (Mattern *et al.*, 2002). (A contrary prediction by Ono *et al.* (2001), that metagabbro should attain neutral buoyancy deep in the lower mantle, seems to depend upon the large amount of low-density, calcium-ferritic-structured, sodic aluminous phase incorporated in their model mineralogy. Thus, although the common mapping of fast-velocity anomalies into low temperatures appears to be a serious oversimplification, in view of the large potential for compositional sources, the usual mapping of fast anomalies into positive density (i.e., negative buoyancy) anomalies does appear to survive in the presence of chemical differentiation.

2.02.6 SUMMARY

The properties of upper-mantle seismic reflectors, especially the observed lateral variations in the seismological properties of the mantle transition zone, indicate that the upper mantle possesses a peridotite composition, approaching

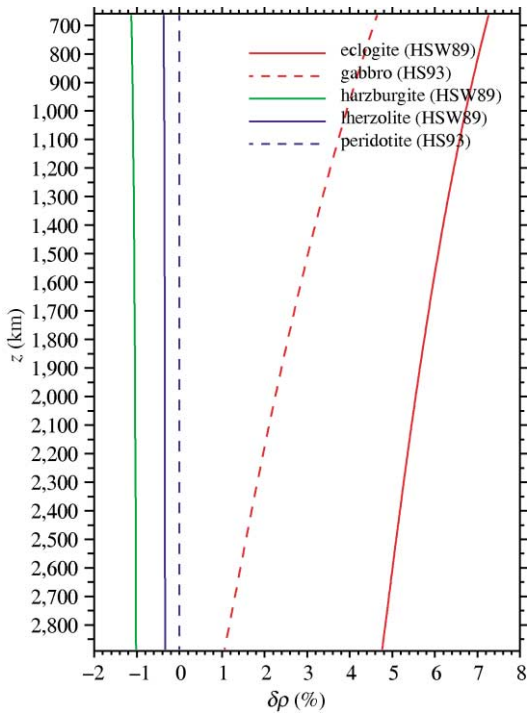


Figure 12 Density anomalies relative to peridotite mantle versus depth: in the lower mantle (blue); for candidate bulk compositions for the basaltic layer (red); and the underlying harzburgite layer (green). Note that the basaltic layer is denser but grows less so with increasing depth.

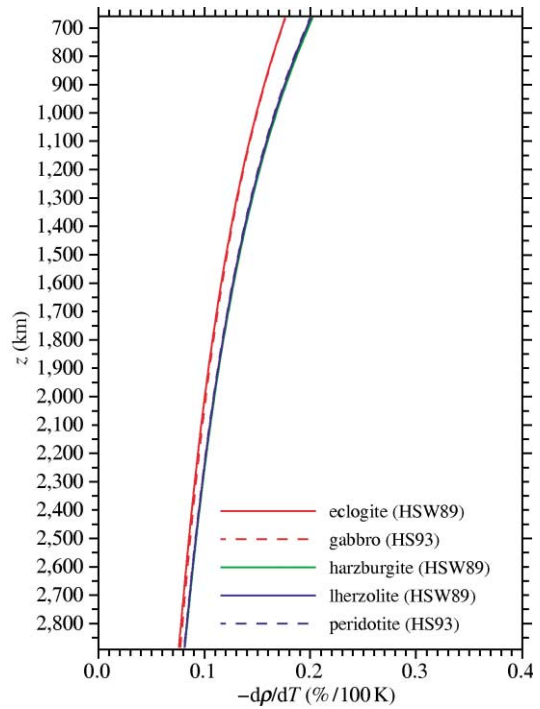


Figure 13 Temperature dependence of density versus depth in the lower mantle: for candidate bulk compositions for the basaltic layer (red); the underlying harzburgite layer (green); and the basal lherzolite (blue). Note that temperature sensitivity falls with increasing depth.

that of the pyrolite model, whose seismic character is largely controlled by thermal perturbations of phase transformations in olivine. Response of seismic character to temperature in the upper mantle may be complicated by local variations in water content or minor variability in Mg/Fe ratios. The role of pyroxene and garnet components in defining seismic character is secondary to that of olivine polymorphs: e.g., dissolution of pyroxene into garnet occurs gradually over more than 100 km, and exsolution of calcium silicate perovskite from garnet–majorite solid solution between 410 km and 660 km depth may overlap with the $\beta \rightarrow \beta + \gamma \rightarrow \gamma$ transformation in olivine.

Subducted basaltic crust is chemically distinct from its surrounding peridotite upper mantle. However, aside from a small signature arising solely from temperature gradients, anhydrous basalt should rapidly become seismically invisible as it sinks below 100–200 km depth. Features exhibiting low seismic velocities in association with the upper surfaces of subducting slabs in the 100–250 km depth range probably arise from hydrous (lawsonite-bearing) metabasalts in the blueschist and eclogite metamorphic regimes. The disappearance of such slow features, and the

occasional appearance of fast velocity anomalies, below 250 km may arise from the passage of silica-saturated eclogites into the stishovite stability field.

The use of seismic tomography to determine the depth of origin of mantle plumes yields conflicting results. Analyses of travel times of seismic boundary-interaction phases, in terms of lateral changes in the absolute depths to the 410 km and 660 km seismic discontinuities, also give rise to seeming inconsistencies, perhaps in part because of the dependence of such methods upon laterally heterogeneous models of shallow mantle structure. The use of (more robust) differential travel times, however, to assess lateral changes in the vertical distance between the 410 km and 660 km seismic discontinuities (i.e., the thickness of the transition zone), suggests that at least some hotspots are associated with thermal plumes which penetrate the entire transition zone.

Densities and bulk sound velocities in the lower mantle are also consistent with the high-pressure mineralogy of a bulk composition approximating an upper-mantle peridotite, such as pyrolite. Seismic constraints provide no support for iron enrichment of the lower mantle relative to such an upper mantle. Silica enrichment of the lower

mantle can be accommodated if the lower mantle is anomalously hot, as would be consistent with a thermal boundary layer of several hundred degrees across a chemical boundary layer. However, silica enrichment alone is unlikely to generate an intrinsic density contrast sufficient to stabilize a chemical boundary layer against convective rehomogenization. Failure to observe the expected seismic signature of such a chemical boundary, in the form of a globally sharp seismic reflector exhibiting significant dynamic topography (>100 km) in the lower mantle, confirms that a peridotite whole mantle that is largely homogeneous in its major element chemistry is most consistent with seismological observations.

Seismic scatterers within the lower mantle are more likely to represent chemical than thermal heterogeneities, with subducted slab material (especially the basaltic crustal component thereof) constituting a likely candidate. The very base of the mantle, nearest the core–mantle boundary, may also be characterized by significant major-element chemical heterogeneity.

REFERENCES

- Agee C. B. (1998) Phase transformations and seismic structure in the upper mantle and transition zone. *Rev. Mineral.* **37**, 165–203.
- Allen R. M., Nolet G., Morgan W. J., Vogfjörd K., Bergsson B. H., Erlendsson P., Foulger G. R., Jakobsdóttir S., Julian B. R., Pritchard M., Ragnarsson S., and Stefánsson R. M. (2002) Imaging the mantle beneath Iceland using integrated seismological techniques. *J. Geophys. Res.* **107**(B12), doi: 10.1029/2001JB000595.
- Anderson D. L. (1979) The upper mantle transition region: Eclogite? *Geophys. Res. Lett.* **6**, 433–436.
- Anderson D. L. (1982) Chemical composition and evolution of the mantle. In *High Pressure Research in Geophysics* (eds. S. Akimoto and M. H. Manghnani). Center for Academic Publication, Tokyo, pp. 301–318.
- Anderson D. L. (1984) The Earth as a planet: paradigms and paradoxes. *Science* **223**, 347–355.
- Anderson D. L. (1989) Composition of the Earth. *Science* **243**, 367–370.
- Anderson D. L. (1994) The sublithospheric mantle as the source of continental flood basalts: the case against the continental lithosphere and plume head reservoirs. *Earth Planet. Sci. Lett.* **123**, 269–280.
- Anderson D. L. (2001) Top-down tectonics? *Science* **293**, 2018–2018.
- Anderson D. L. and Bass J. D. (1984) Mineralogy and composition of the upper mantle. *Geophys. Res. Lett.* **11**, 637–640.
- Anderson D. L. and Bass J. D. (1986) Transition region of the Earth's upper mantle. *Nature* **320**, 321–328.
- Bass J. D. and Anderson D. L. (1984) Composition of the upper mantle: geophysical tests of two petrological models. *Geophys. Res. Lett.* **11**, 229–232.
- Bina C. R. (1993) Mutually consistent estimates of upper mantle composition from seismic velocity contrasts at 400 km depth. *Pure Appl. Geophys.* **141**, 101–109.
- Bina C. R. (1998a) Olivine emerges from isolation. *Nature* **392**, 650–653.
- Bina C. R. (1998b) Lower mantle mineralogy and the geophysical perspective. *Rev. Mineral.* **37**, 205–239.
- Bina C. R. (1998c) Free energy minimization by simulated annealing with applications to lithospheric slabs and mantle plumes. *Pure Appl. Geophys.* **151**, 605–618.
- Bina C. R. (2002) Phase transition complexity and multiple seismic reflectors in subduction zones. *Eos, Trans., AGU* **83**(47), Fall Meet. Suppl., Abstract S52C-05.
- Bina C. R. and Helffrich G. R. (1992) Calculation of elastic properties from thermodynamic equation of state principles. *Ann. Rev. Earth Planet. Sci.* **20**, 527–552.
- Bina C. R. and Helffrich G. (1994) Phase transition Clapeyron slopes and transition zone seismic discontinuity topography. *J. Geophys. Res.* **99**, 15853–15860.
- Bina C. R. and Kumazawa M. (1993) Thermodynamic coupling of phase and chemical boundaries in planetary interiors. *Phys. Earth Planet. Inter.* **76**, 329–341.
- Bina C. R. and Liu M. (1995) A note on the sensitivity of mantle convection models to composition-dependent phase relations. *Geophys. Res. Lett.* **22**, 2565–2568.
- Bina C. R. and Silver P. G. (1990) Constraints on lower mantle composition and temperature from density and bulk sound velocity profiles. *Geophys. Res. Lett.* **17**, 1153–1156.
- Bina C. R. and Silver P. G. (1997) Bulk sound travel times and implications for mantle composition and outer core heterogeneity. *Geophys. Res. Lett.* **24**, 499–502.
- Bina C. R. and Wood B. J. (1987) The olivine–spinel transitions: experimental and thermodynamic constraints and implications for the nature of the 400 km seismic discontinuity. *J. Geophys. Res.* **92**, 4853–4866.
- Bina C. R. and Wood B. J. (2000) Thermal and compositional implications of seismic velocity anomalies in the lower mantle. *Eos, Trans., AGU* **81**(22), Western Pacific Suppl., Abstract T32B-03, pp. WP193–WP194.
- Birch F. (1952) Elasticity and constitution of the Earth's interior. *J. Geophys. Res.* **57**, 227–286.
- Brodholt J. P. (2000) Pressure-induced changes in the compression mechanism of aluminous perovskite in the Earth's mantle. *Nature* **407**, 620–622.
- Castle J. C. and Creager K. C. (1999) A steeply dipping discontinuity in the lower mantle beneath Izu-Bonin. *J. Geophys. Res.* **104**, 7279–7292.
- Chevrot S., Vinnik L., and Montagner J.-P. (1999) Global-scale analysis of the mantle Pds phases. *J. Geophys. Res.* **104**, 20203–20220.
- Christiansen R. L., Foulger G. R., and Evans J. R. (2002) Upper-mantle origin of the Yellowstone hotspot. *Geol. Soc. Am. Bull.* **114**, 1245–1256.
- Connolly J. A. D. and Kerrick D. M. (2002) Metamorphic controls on seismic velocity of subducted oceanic crust at 100–250 km depth. *Earth Planet. Sci. Lett.* **204**, 61–74.
- Deuss A. and Woodhouse J. H. (2001) Seismic observations of splitting of the mid-mantle transition zone discontinuity in Earth's mantle. *Science* **294**, 354–357.
- Deuss A. and Woodhouse J. H. (2002) A systematic search for mantle discontinuities using SS-precursors. *Geophys. Res. Lett.* **29**(8), doi: 10.1029/2002GL014768.
- Dueker K. G. and Sheehan A. F. (1997) Mantle discontinuity structure from midpoint stacks of converted P and S waves across the Yellowstone hotspot track. *J. Geophys. Res.* **102**, 8313–8328.
- Duffy T. S. and Anderson D. L. (1989) Seismic velocities in mantle minerals and the mineralogy of the upper mantle. *J. Geophys. Res.* **94**, 1895–1912.
- Duffy T. S., Zha C. S., Downs R. T., Mao H. K., and Hemley R. J. (1995) Elasticity of forsterite to 16 GPa and the composition of the upper mantle. *Nature* **378**, 170–173.
- Fei Y., Mao H.-K., and Mysen B. O. (1991) Experimental determination of element partitioning and calculation of phase relations in the MgO–FeO–SiO₂ system at high pressure and high temperature. *J. Geophys. Res.* **96**, 2157–2169.

- Fei Y., Mao H.-K., Shu J., and Hu J. (1992) P - V - T equation of state of magnesio-wüstite ($\text{Mg}_{0.6}\text{Fe}_{0.4}\text{O}$). *Phys. Chem. Min.* **18**, 416–422.
- Fiquet G., Dewaele A., Andrault D., Kunz M., and LeBihan T. (2000) Thermoelastic properties and crystal structure of MgSiO_3 perovskite at lower mantle pressure and temperature conditions. *Geophys. Res. Lett.* **27**, 21–24.
- Flesch L. M., Li B., and Liebermann R. C. (1998) Sound velocities of polycrystalline MgSiO_3 -orthopyroxene to 10 GPa at room temperature. *Am. Mineral.* **83**, 444–450.
- Foulger G. R., Pritchard M. J., Julian B. R., Evans J. R., Allen R. M., Nolet G., Morgan W. J., Bergsson B. H., Erlendsson P., Jakobsdottir S., Ragnarsson S., Stefansson R., and Vogfjörð K. (2001) Seismic tomography shows that upwelling beneath Iceland is confined to the upper mantle. *Geophys. J. Int.* **146**, 504–530.
- Fukao Y., Widiyantoro S., and Obayashi M. (2001) Stagnant slabs in the upper and lower mantle transition region. *Rev. Geophys.* **39**, 291–323.
- Garlick G. D. (1969) Consequences of chemical equilibrium across phase changes in the mantle. *Lithos* **2**, 325–331.
- Garnero E. J. (2000) Heterogeneity of the lowermost mantle. *Ann. Rev. Earth Planet. Sci.* **28**, 509–537.
- Green H. W., II and Houston H. (1995) The mechanics of deep earthquakes. *Ann. Rev. Earth Planet. Sci.* **23**, 169–213.
- Gu Y. J. and Dziewonski A. M. (2002) Global variability of transition zone thickness. *J. Geophys. Res.* **107**(B7), doi: 10.1029/2001JB000489.
- Hacker B. R. (1996) Eclogite formation and the rheology, buoyancy, seismicity, and H_2O content of oceanic crust. In *Subduction: Top to Bottom*, Geophys. Monogr. 96 (eds. G. Bebout, D. Scholl, S. Kirby, and J. Platt). AGU, Washington, DC, pp. 337–346.
- Hedlin M. A. H., Shearer P. M., and Earle P. S. (1997) Seismic evidence for small-scale heterogeneity throughout the Earth's mantle. *Nature* **387**, 145–150.
- Helfrich G. (1996) Subducted lithospheric slab velocity structure: observations and mineralogical inferences. In *Subduction: Top to Bottom*, Geophys. Monogr. 96 (eds. G. Bebout, D. Scholl, S. Kirby, and J. Platt). AGU, Washington, DC, pp. 215–222.
- Helfrich G. and Bina C. R. (1994) Frequency dependence of the visibility and depths of mantle seismic discontinuities. *Geophys. Res. Lett.* **21**, 2613–2616.
- Helfrich G. and Stein S. (1993) Study of the structure of the slab-mantle interface using reflected and converted seismic waves. *Geophys. J. Int.* **115**, 14–40.
- Helfrich G., Stein S., and Wood B. J. (1989) Subduction zone thermal structure and mineralogy and their relationship to seismic wave reflections and conversions at the slab/mantle interface. *J. Geophys. Res.* **94**, 753–763.
- Helfrich G., Asencio E., Knapp J., and Owens T. (2003) Transition zone structure under the northern North Sea. *Geophys. J. Int.* (in press).
- Helfrich G. R. (2000) Topography of the transition zone seismic discontinuities. *Rev. Geophys.* **38**, 141–158.
- Helfrich G. R. and Wood B. J. (1996) 410-km discontinuity sharpness and the form of the olivine α - β phase diagram: resolution of apparent seismic contradictions. *Geophys. J. Int.* **126**, F7–F12.
- Helfrich G. R. and Wood B. J. (2001) The Earth's mantle. *Nature* **412**, 501–507.
- Hirose K., Fei Y., Ma Y., and Mao H.-K. (1999) The fate of subducted basaltic crust in the Earth's lower mantle. *Nature* **397**, 53–56.
- Humphreys E. D., Dueker K. G., Schutt D. L., and Smith R. B. (2000) Beneath Yellowstone: evaluating plume and non-plume models using teleseismic images of the upper mantle. *GSA Today* **10**(12), 1–7.
- Irfune T. and Isshiki M. (1998) Iron partitioning in a pyrolite mantle and the nature of the 410-km seismic discontinuity. *Nature* **392**, 702–705.
- Ita J. J. and Stixrude L. (1992) Petrology, elasticity and composition of the transition zone. *J. Geophys. Res.* **97**, 6849–6866.
- Jackson I. (1983) Some geophysical constraints on the chemical composition of the Earth's lower mantle. *Earth Planet. Sci. Lett.* **62**, 91–103.
- Jackson I. (1998) Elasticity, composition and temperature of the Earth's lower mantle: a reappraisal. *Geophys. J. Int.* **134**, 291–311.
- James D. E., Boyd F. R., Bell D., and Carlson R. (2001) Xenolith constraints on seismic velocities in the upper mantle beneath southern Africa. Abstracts of the Slave-Kaapvaal Workshop "A Tale of Two Cratons," Merrickville, Ontario, Canada, 2pp.
- Jeanloz J. (1995) Earth dons a different mantle. *Nature* **378**, 130–131.
- Jeanloz J. and Knittle E. (1989) Density and composition of the lower mantle. *Phil. Trans. Roy. Soc. London A* **328**, 377–389.
- Kaneshima S. and Helfrich G. (1998) Detection of lower mantle scatterers northeast of the Mariana subduction zone using short-period array data. *J. Geophys. Res.* **103**, 4825–4838.
- Kaneshima S. and Helfrich G. (1999) Dipping low-velocity layer in the mid-lower mantle: evidence for geochemical heterogeneity. *Science* **283**, 1888–1892.
- Karki B. B., Stixrude L., and Crain J. (1997) *Ab initio* elasticity of three high-pressure polymorphs of silica. *Geophys. Res. Lett.* **24**, 3269–3272.
- Katsura T. and Ito E. (1989) The system Mg_2SiO_4 - Fe_2SiO_4 at high pressures and temperatures: precise determination of stabilities of olivine, modified spinel, and spinel. *J. Geophys. Res.* **94**, 15663–15670.
- Keller W. R., Anderson D. L., and Clayton R. W. (2000) Resolution of tomographic models of the mantle beneath Iceland. *Geophys. Res. Lett.* **27**, 3993–3996.
- Kennett B. L. N., Engdahl E. R., and Buland R. (1995) Constraints on seismic velocities in the Earth from traveltimes. *Geophys. J. Int.* **122**, 108–124.
- Kerr R. A. (2003) Plumes from the core lost and found. *Science* **299**, 35–36.
- Kesson S. E., Fitzgerald J. D., and Shelley J. M. G. (1998) Mineralogy and dynamics of a pyrolite lower mantle. *Nature* **393**, 252–255.
- Kind R., Li X., Yuan X., Sobolev S. V., Hanka W., Ramesh S. D., Gu Y. G., and Dziewonski A. M. (2002) Global comparison of SS precursor and Ps conversion data from the upper mantle seismic discontinuities. *Eos, Trans., AGU* **83**(47), Fall Meet. Suppl., Abstract S52C-07.
- Kumazawa M., Sawamoto H., Ohtani E., and Masaki K. (1974) Post-spinel phase of forsterite and evolution of the Earth's mantle. *Nature* **247**, 356–358.
- Lebedev S., Chevrot S., and van der Hilst R. D. (2002) Seismic evidence for olivine phase changes at the 410- and 660-kilometer discontinuities. *Science* **296**, 1300–1302.
- Li B., Rigden S. M., and Liebermann R. C. (1996) Elasticity of stishovite at high pressure. *Phys. Earth Planet. Inter.* **96**, 113–127.
- Li B., Liebermann R. C., and Weidner D. J. (2001) P - V - V_p - V_s - T measurements on wadsleyite to 7 GPa and 873 K: implications for the 410-km seismic discontinuity. *J. Geophys. Res.* **106**, 30575–30591.
- Li X., Kind R., Priestley K., Sobolev S. V., Tilmann F., Yuan X., and Weber M. (2000) Mapping the Hawaiian plume conduit with converted seismic waves. *Nature* **405**, 938–941.
- Liu J., Topor L., Zhang J., Navrotsky A., and Liebermann R. C. (1996) Calorimetric study of the coesite-stishovite

- transformation and calculation of the phase boundary. *Phys. Chem. Min.* **23**, 11–16.
- Liu M. (1994) Asymmetric phase effects and mantle convection patterns. *Science* **264**, 1904–1907.
- Liu Z.-K. and Ågren J. (1995) Thermodynamics of constrained and unconstrained equilibrium systems and their phase rules. *J. Phase Equil.* **16**, 30–35.
- Mao H. K., Shen G., and Hemley R. J. (1997) Multivariable dependence of Fe/Mg partitioning in the Earth's lower mantle. *Science* **278**, 2098–2100.
- Mattern E., Matas J., and Ricard Y. (2002) Computing density and seismic velocity of subducting slabs. *Eos, Trans., AGU* **83**(47), Fall Meet. Suppl., Abstract S51A-1011.
- McCammon C. A. (1997) Perovskite as a possible sink for ferric iron in the lower mantle. *Nature* **387**, 694–696.
- McDonough W. F. and Rudnick R. L. (1998) Mineralogy and composition of the upper mantle. *Rev. Mineral.* **37**, 139–164.
- Melbourne T. and Helmberger D. (1998) Fine structure of the 410-km discontinuity. *J. Geophys. Res.* **103**, 10091–10102.
- Montagner J.-P. and Ritsema J. (2001) Interactions between ridges and plumes. *Science* **294**, 1472–1473.
- Neele F., de Regt H., and VanDecar J. (1997) Gross errors in upper-mantle discontinuity topography from underside reflection data. *Geophys. J. Int.* **129**, 194–204.
- Niu F. and Kawakatsu H. (1997) Depth variation of the mid-mantle seismic discontinuity. *Geophys. Res. Lett.* **24**, 429–432.
- Niu F., Solomon S. C., Silver P. G., Suetsugu D., and Inoue H. (2002) Mantle transition-zone structure beneath the South Pacific Superswell and evidence for a mantle plume underlying the Society hotspot. *Earth Planet. Sci. Lett.* **198**, 371–380.
- Ono S. and Yasuda A. (1996) Compositional change of majoritic garnet in a MORB composition from 7 to 17 GPa and 1,400 to 1,600 °C. *Phys. Earth Planet. Inter.* **96**, 171–179.
- Ono S., Ito E., and Katsura T. (2001) Mineralogy of subducted basaltic crust (MORB) from 25 to 37 GPa and chemical heterogeneity of the lower mantle. *Earth Planet. Sci. Lett.* **190**, 57–63.
- Peacock S. M. (1993) The importance of blueschist → eclogite dehydration reactions in subducting oceanic crust. *Geol. Soc. Am. Bull.* **105**, 684–694.
- Pognante U. (1989) Tectonic implications of lawsonite formation in the Sesia zone (western Alps). *Tectonophysics* **162**, 219–227.
- Reinsch D. (1979) Glaucofanites and eclogites from Val Chiusella, Sesia-Lanzo zone (Italian Alps). *Contrib. Mineral. Petrol.* **70**, 257–266.
- Ringwood A. E. (1975) *Composition and Petrology of the Earth's Mantle*. McGraw-Hill, New York.
- Ringwood A. E. (1989) Constitution and evolution of the mantle. *Spec. Publ. Geol. Soc. Australia* **14**, 457–485.
- Ritsema J., van Heijst H. J., and Woodhouse J. H. (1999) Complex shear wave velocity structure imaged beneath Africa and Iceland. *Science* **286**, 1925–1928.
- Saltzer R. L. and Humphreys E. D. (1997) Upper mantle P wave velocity structure of the eastern Snake River Plain and its relationship to geodynamic models of the region. *J. Geophys. Res.* **102**, 11829–11841.
- Shearer P. M. and Flanagan M. P. (1999) Seismic velocity and density jumps across the 410- and 660-kilometer discontinuities. *Science* **285**, 1545–1548.
- Shearer P. M., Flanagan M. P., Reif C., and Masters G. (2002) Seismic constraints on mantle discontinuities: what we know and what we don't know. *Eos, Trans., AGU* **83**(47), Fall Meet. Suppl., Abstract S52C-08.
- Shen Y., Solomon S. C., Bjarnason I. T., and Wolfe C. J. (1998) Seismic evidence for a lower mantle origin of the Iceland plume. *Nature* **395**, 62–65.
- Sinogeikin S. V., Katsura T., and Bass J. D. (1998) Sound velocities and elastic properties of Fe-bearing wadsleyite and ringwoodite. *J. Geophys. Res.* **103**, 20819–20825.
- Smyth J. R. and Frost D. J. (2002) The effect of water on the 410-km discontinuity: an experimental study. *Geophys. Res. Lett.* **29**(10), doi: 10.1029/2001GL014418.
- Solomatov V. S. and Stevenson D. J. (1994) Can sharp seismic discontinuity be caused by non-equilibrium phase transformation? *Earth Planet. Sci. Lett.* **125**, 267–279.
- Stixrude L. (1997) Structure and sharpness of phase transitions and mantle discontinuities. *J. Geophys. Res.* **102**, 14835–14852.
- Stixrude L., Hemley R. J., Fei Y., and Mao H. K. (1992) Thermoelasticity of silicate perovskite and magnesiowüstite stratification of the Earth's mantle. *Science* **257**, 1099–1101.
- Takenaka S., Sanshadokoro H., and Yoshioka S. (1999) Velocity anomalies and spatial distributions of physical properties in horizontally lying slabs beneath the North-western Pacific region. *Phys. Earth Planet. Inter.* **112**, 137–157.
- Vacher P., Mocquet A., and Sotin C. (1998) Computation of seismic profiles from mineral physics: the importance of the non-olivine components for explaining the 660 km depth discontinuity. *Phys. Earth Planet. Inter.* **106**, 275–298.
- Vacher P., Spakman W., and Wortel M. J. R. (1999) Numerical tests on the seismic visibility of metastable minerals in subduction zones. *Earth Planet. Sci. Lett.* **170**, 335–349.
- VanDecar J. C., James D. E., and Assumpção M. (1995) Seismic evidence for a fossil mantle plume beneath South America and implications for plate driving forces. *Nature* **378**, 25–31.
- van der Lee S., Paulssen H., and Nolet G. (1994) Variability of P660s phases as a consequence of topography on the 660 km discontinuity. *Phys. Earth Planet. Inter.* **86**, 147–164.
- van der Meijde M., Marone F., van der Lee S., and Giardini D. (2002) Seismological evidence for the presence of water near the 410 km discontinuity. *Eos, Trans., AGU* **83**(47), Fall Meet. Suppl., Abstract S52C-03.
- Vinnik L., Chevrot S., and Montagner J.-P. (1997) Evidence for a stagnant plume in the transition zone? *Geophys. Res. Lett.* **24**, 1007–1010.
- Walck M. C. (1984) The P-wave upper mantle structure beneath an active spreading center: the Gulf of California. *Geophys. J. Roy. Astro. Soc.* **76**, 697–723.
- Walker D. and Agee C. (1989) Partitioning “equilibrium,” temperature gradients, and constraints on Earth differentiation. *Earth Planet. Sci. Lett.* **96**, 49–60.
- Wang Y., Weidner D. J., and Guyot F. (1996) Thermal equation of state of CaSiO₃ perovskite. *J. Geophys. Res.* **101**, 661–672.
- Weidner D. J. (1986) Mantle model based on measured physical properties of minerals. In *Chemistry and Physics of Terrestrial Planets* (ed. S. K. Saxena). Springer, New York, pp. 251–274.
- Wolfe C. J., Bjarnason I. T., VanDecar J. C., and Solomon S. C. (1997) Seismic structure of the Iceland mantle plume. *Nature* **385**, 245–247.
- Wood B. J. (1987) Thermodynamics of multicomponent systems containing several solid solutions. *Rev. Mineral.* **17**, 71–95.
- Wood B. J. (1995) The effect of H₂O on the 410-kilometer seismic discontinuity. *Science* **268**, 74–76.
- Wood B. J. (2000) Phase transformations and partitioning relations in peridotite under lower mantle conditions. *Earth Planet. Sci. Lett.* **174**, 341–354.
- Wood B. J. and Rubie D. C. (1996) The effect of alumina on phase transformations at the 660-kilometer discontinuity from Fe–Mg partitioning experiments. *Science* **273**, 1522–1524.
- Wood B. J., Pawley A., and Frost D. R. (1996) Water and carbon in the Earth's mantle. *Phil. Trans. Roy. Soc. London A* **354**, 1495–1511.
- Zha C.-S., Duffy T. S., Downs R. T., Mao H.-K., and Hemley R. J. (1998a) Brillouin scattering and X-ray diffraction of San Carlos olivine: direct pressure determination to 32 GPa. *Earth Planet. Sci. Lett.* **159**, 25–33.

- Zha C.-S., Duffy T. S., Downs R. T., Mao H.-K., Hemley R. J., and Weidner D. J. (1988b) Single crystal elasticity of the α and β of Mg_2SiO_4 polymorphs at high pressure. In *Properties of Earth and Planetary Materials at High Pressure and Temperature*, Geophys. Monogr. 101 (eds. M. H. Manghnani and T. Yagi). AGU, Washington, DC, pp. 9–16.
- Zhang J. and Weidner D. J. (1999) Thermal equation of state of aluminum-enriched silicate perovskite. *Science* **284**, 782–784.
- Zhao Y. and Anderson D. L. (1994) Mineral physics constraints on the chemical composition of the Earth's lower mantle. *Phys. Earth Planet. Inter.* **85**, 273–292.